Newton

Article

Three-dimensional mapping of electrical behavior in perovskite films using tomographic conductive atomic force microscopy

Graphical abstract

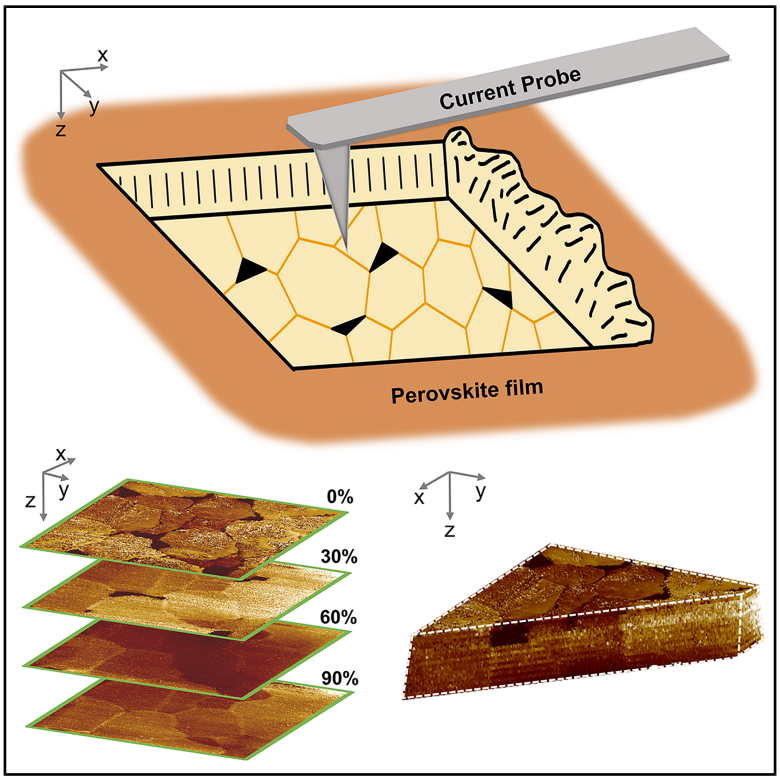

Highlights

- TC-AFM maps current in perovskite films at different depths during material removal
- 3D volume reconstruction reveals vertical current variation within the film
- Quantitative analysis shows conductivity differences among passivation treatments
- Multiple characterization methods validate the reliability of proposed technique

Authors

Minghui Li, Pengfei Wu, Jiali Liu, ..., Yaxin Zhai, Fei Zhang, Chuanxiao Xiao

Correspondence

yzhai@hunnu.edu.cn (Y.Z.), fei_zhang@tju.edu.cn (F.Z.), cxiao@nimte.ac.cn (C.X.)

In brief

Passivation treatments are widely used in perovskite solar cells. By using three-dimensional tomographic conductive atomic force microscopy to examine current distribution and to quantify high-resistance regions in perovskite films with different passivation strategies, Li et al. reveal how bulk passivation enhances conductivity throughout the film. They also show that surface passivation improves near-surface properties, offering a powerful tool for analyzing passivation effects and enabling improvements in film quality and optimized device performance in perovskite technologies.

Li et al., 2026, Newton *2*, 100367
April 6, 2026 © 2025 The Author(s). Published by Elsevier Inc.
https://doi.org/10.1016/j.newton.2025.100367

CellPress

Please cite this article in press as: Li et al., Three-dimensional mapping of electrical behavior in perovskite films using tomographic conductive atomic force microscopy, Newton (2025), https://doi.org/10.1016/j.newton.2025.100367

Newton

CellPress
OPEN ACCESS

Article

Three-dimensional mapping of electrical behavior in perovskite films using tomographic conductive atomic force microscopy

Minghui Li,[1,2,8] Pengfei Wu,[3,4,8] Jiali Liu,[5] Xiting Lang,[1] Yating Shi,[3] Xirui Liu,[1,2] Hao Tian,[1] Yongjie Jiang,[1] Yangyang Gou,[1] Yueying Zhang,[1] Zhenhai Yang,[6] Jichun Ye,[1] Yaxin Zhai,[5,*] Fei Zhang,[3,*] and Chuanxiao Xiao[1,7,9,*]

[1]Ningbo Institute of Materials Technology and Engineering, Chinese Academy of Sciences, Ningbo 315201, China
[2]School of Materials Science and Chemical Engineering, Ningbo University, Ningbo 315211, China
[3]School of Chemical Engineering and Technology, Tianjin University, Tianjin 300072, China
[4]Petrochemical Research Institute, PetroChina Company Limited, Beijing 102206, China
[5]Key Laboratory of Low-Dimensional Quantum Structures and Quantum Control of Ministry of Education, Department of Physics, Hunan Normal University, Changsha 410081, China
[6]School of Optoelectronic Science and Engineering & Collaborative Innovation Center of Suzhou Nano Science and Technology, Soochow University, Suzhou 215006, China
[7]Ningbo New Materials Testing and Evaluation Center Co., Ltd., Ningbo 315201, China
[8]These authors contributed equally
[9]Lead contact
*Correspondence: yzhai@hunnu.edu.cn (Y.Z.), fei_zhang@tju.edu.cn (F.Z.), cxiao@nimte.ac.cn (C.X.)
https://doi.org/10.1016/j.newton.2025.100367

ACCESSIBLE OVERVIEW Effective passivation treatments are widely used in perovskite solar cells to mitigate defects in perovskite materials. However, current microscopy techniques for assessing passivation effects are often limited to surface analysis. In this study, we use contact-mode tomographic conductive atomic force microscopy to map the current distribution within perovskite films as they are progressively removed. This technique reveals the internal current distribution across perovskite films subjected to various passivation treatments. By reconstructing three-dimensional current images, we generate a current volume, with vertical slices providing detailed insight into the evolution of high-resistance regions within the films. Through quantitative analysis, we compare the internal current distributions and potential defects in untreated, bulk-treated, surface-treated, and combination-treated samples. Comprehensive film and device characterizations further validate the reliability of our method. This work introduces a robust and versatile tool for analyzing passivation effects in perovskite materials, offering opportunities to improve film quality and optimize device performance in perovskite technologies.

SUMMARY

Passivation treatments are crucial for improving the performance of perovskite solar cells by reducing nonradiative recombination and enhancing charge transport. However, their microscopic effects within the perovskite films remain unclear due to limitations of conventional characterization methods. This study uses three-dimensional tomographic conductive atomic force microscopy to examine the structural and electrical properties of perovskite films treated with different passivation strategies. Through 3D current mapping and quantitative analysis, we identify internal electrical pathways and structural defects. While untreated films exhibit high-resistance regions that hinder carrier transport, bulk passivation reduces these regions, particularly in the film interior, thereby enhancing grain boundary conductivity. Surface passivation primarily mitigates near-surface defects, improving local conductivity. Combining both strategies results in a more conductive internal structure, with high-resistance regions confined to the top surface. These findings highlight how passivation treatments improve perovskite film quality, directly correlating with enhanced solar cell performance.

This is an open access article under the CC BY license (http://creativecommons.org/licenses/by/4.0/).

Please cite this article in press as: Li et al., Three-dimensional mapping of electrical behavior in perovskite films using tomographic conductive atomic force microscopy, Newton (2025), https://doi.org/10.1016/j.newton.2025.100367

INTRODUCTION

Perovskite-based optoelectronic materials offer significant advantages, including tunable material properties,[1–4] potential for low-cost manufacturing, and simple fabrication processes,[5,6] that enable high device performance. These attributes have positioned perovskite materials as some of the most promising candidates for photovoltaic applications. However, the commonly used solution-processing techniques often lead to detrimental defects within the perovskite layer, resulting from rapid nucleation and crystal growth.[7,8] Additionally, defects can develop at the interfaces during subsequent device fabrication.[9,10] These defects frequently act as non-radiative recombination centers, hindering carrier separation and transport, significantly limiting the performance and stability of perovskite solar cells (PSCs). Therefore, minimizing these defects is essential for achieving high efficiency and long-term reliability in PSCs.

Various passivation techniques have been developed to address this challenge, including surface and bulk passivation strategies, which effectively reduce internal defects in the material.[11–14] Some studies have even combined surface and bulk passivation treatments to further enhance device performance.[15–18] Although passivation techniques have been shown to improve device performance, the mechanisms underlying the internal structure of perovskite films remain poorly understood. Traditional characterization methods, which are typically macroscopic and indirect, provide limited insight into the microscopic behavior of these materials.

In this study, we apply tomographic conductive atomic force microscopy (TC-AFM) to investigate the electrical properties of perovskite films, enabling three-dimensional (3D) mapping and quantitative analysis of current distribution within materials.[19–23] Using a high-elastic-modulus conductive probe in contact mode, we can perform *in situ*, layer-by-layer removal of the perovskite material, enabling detailed 3D mapping of the current distribution across the film. Our findings reveal that untreated perovskite films contain large-volume, high-resistance regions that serve as non-radiative recombination centers, impeding carrier transport. In contrast, surface and bulk passivation treatments reduce the extent of these high-resistance regions and improve conductivity at the grain boundaries (GBs). The most significant results are observed in the combined surface- and bulk passivation-treated films, where nearly all high-resistance regions disappear, resulting in a highly conductive internal structure. These findings correlate with improved film quality and device performance, confirming that 3D TC-AFM is a powerful tool for understanding the microscopic mechanisms behind perovskite passivation treatments and their impact on solar cell performance.

RESULTS

3D tomographic technique for depth-resolved electrical mapping

Figure 1 illustrates the experimental setup for performing tomographic experiments on perovskite materials using TC-AFM and the 3D current volume obtained at different depths. As shown in Figure 1A, controlling the force applied by the conductive probe to the sample (glass/indium tin oxide (ITO)/$FAPbI_3$) enables uniform removal of the perovskite layer. The material removal thickness per scan is determined based on the film thickness and the actual number of scans. For samples with different passivation treatments, the applied force is slightly adjusted to achieve a comparable number of tomographic layers, ensuring similar milling rates across all films. Initially, the probe reduces the surface

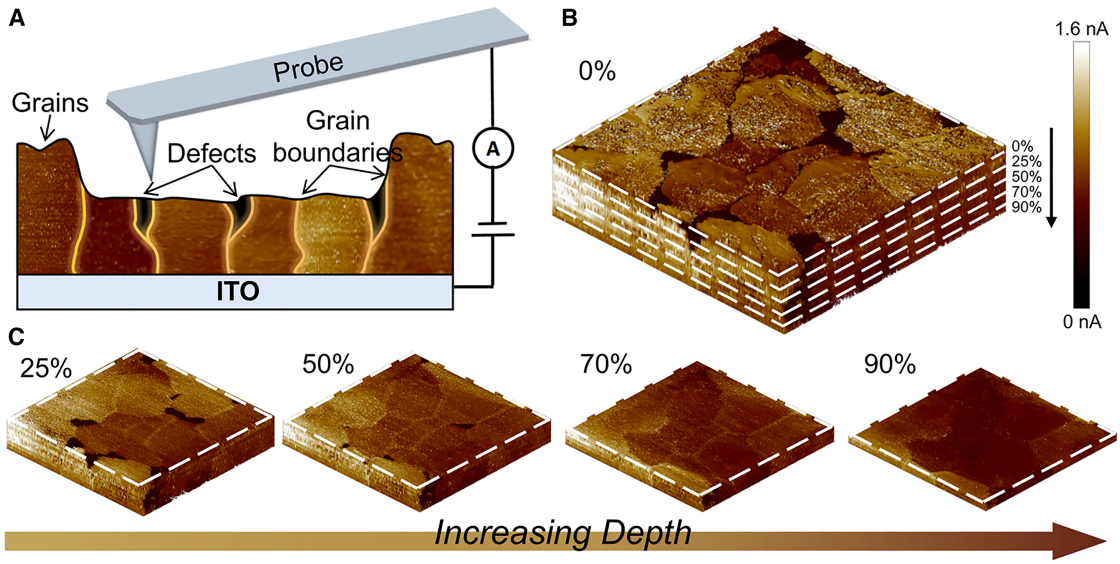

Figure 1. Schematic of the tomographic method and 3D reconstruction of current mapping

(A) Illustration of continuous nanomachining by the probe.

(B) 3D current volume of the sample after reconstruction.

(C) 3D current volumes obtained by cutting along the dashed line in (B) at depths of 25%, 50%, 70%, and 90%. The current scale in all 3D volumes ranges from 0 to 1.6 nA.

Please cite this article in press as: Li et al., Three-dimensional mapping of electrical behavior in perovskite films using tomographic conductive atomic force microscopy, Newton (2025), https://doi.org/10.1016/j.newton.2025.100367

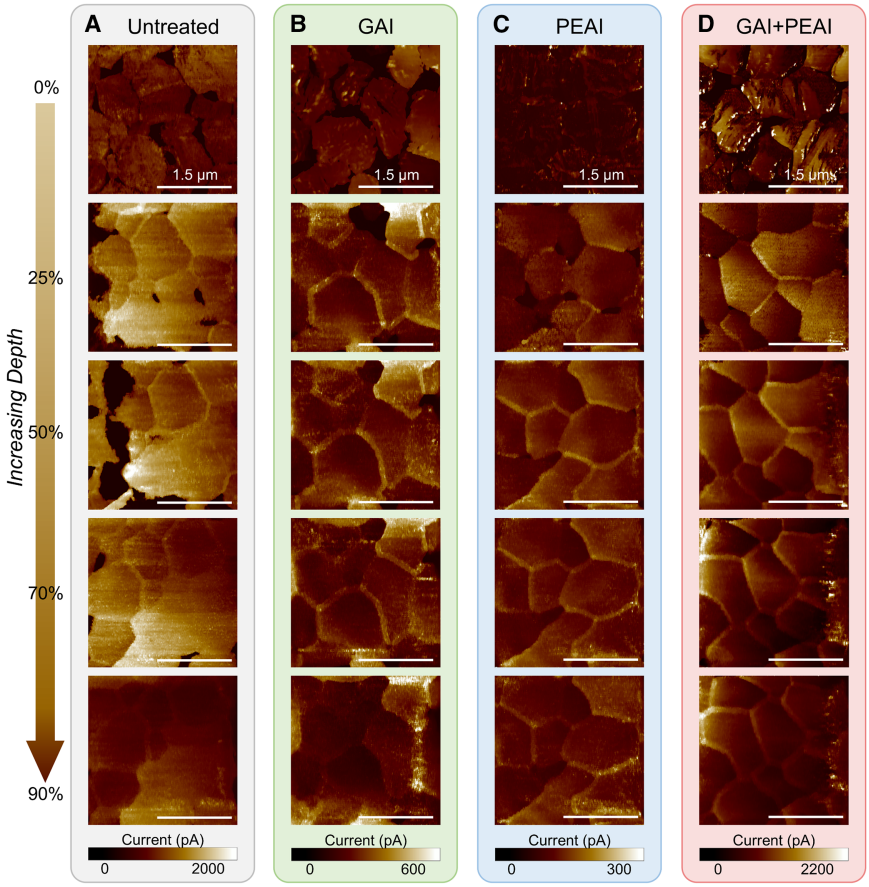

Figure 2. 2D current maps of perovskite samples at different tomographic depths

The gray, green, blue, and red boxes correspond to the (A) untreated, (B) GAI-treated, (C) PEAI-treated, and (D) GAI+PEAI-treated samples, respectively. Each box shows the 2D current images acquired at depths of 0%, 25%, 50%, 70%, and 90%.

roughness, as the typical roughness of perovskite films is less than 50 nm,[24] and a flat surface is achieved after a few scans. After the scans, we observe material accumulation at the edge and a dent by scanning a slightly larger area (Figure S1). Previous studies have reported that debris generated during material removal can affect the tomography data in the scanned region.[25,26] In this study, we carefully monitor both atomic force microscopy (AFM) and conductive AFM (C-AFM) images throughout the process to avoid interference from debris and probe contamination, ensuring the reliability of the tomography data. During the removal process, lateral 2D current images are captured at multiple depths, enabling reconstruction of a 3D current volume, as illustrated in Figures 1B and 1C. Cross-sectional images extracted from this 3D current volume enable us to analyze changes in the conductive characteristics along the vertical direction, as demonstrated in Figure S2. This highlights the power of TC-AFM in revealing the internal micro-properties of materials. The 3D nature of TC-AFM provides a detailed electrical analysis, both laterally and vertically, offering a comprehensive view of current performance at various depths (see Videos S1 and S2 for better visualization). Additional C-AFM measurements conducted under controlled illumination conditions indicate that illumination does not affect the conductivity distribution (Figure S3). As shown in Figure S4, the average current under illumination increases by approximately 2–3 times compared to that under dark conditions, while the spatial distribution remained unchanged. This indicates that, while the carrier concentration increases under illumination, the local conductive pathways remain unaltered,[27] and, thus, illumination was not applied in the rest scans.

Depth-resolved current mapping and analysis

The 2D current maps, acquired layer by layer, reveal significant electrical behavior in the four different passivation treatments of $FAPbI_3$ thin films: untreated, bulk passivation with guanidinium iodide (GAI), surface passivation with phenylethylammonium iodide (PEAI), and combined bulk and surface passivation (GAI+PEAI). Figure 2 shows selective current images from 0% to 90% depth as the material is progressively removed (also see Videos S3, S4, S5, and S6). The untreated perovskite sample's tomographic current images reveal numerous complex high-resistance regions within the film (Figure 2A). When combined with the surface topography (Figure S5A), it is evident that the current at or around the GBs is near zero, appearing as dark regions. The dark regions correspond to areas with high resistance or low conductivity. These areas correspond to low-conductivity regions, likely due to lower carrier density at the GBs, as reported in a previous study.[28] Another previous study has shown that high-resistance regions in C-AFM measurements are associated with low-conductivity PbI_2.[29] As the material is progressively removed, the extent of these high-resistance regions increases. The high-resistance regions within the perovskite material impede charge-carrier transport, which may be related to defects. At a 50% removal depth, the high-resistance regions occupy the most significant proportion of the film. Figure S6 and Table S1 show the fraction of high-resistance regions at different depths. For the untreated sample, when the removal depth reached 50%, the proportion of high-resistance regions is significantly higher than that at the sample surface. However, as the material removal continues, these regions decrease, with none present at a 90% removal depth. Importantly, the high resistance does not originate from topographical features such as pinholes but, rather, from the material's inherent conductivity (Figure S7).

For the perovskite film with bulk passivation using GAI, the current map shows a more uniform current distribution

compared to the untreated sample, with a significant reduction in high-resistance regions (Figure 2B). The GAI-treated sample shows a significantly reduced fraction of dark regions at 25% and 50% depth compared to the untreated sample (Figure S6F). Similarly, derivative analysis of the depth-resolved current variations (Figure S8D) demonstrates that the GAI-treated sample exhibits much smaller vertical current changes than the untreated sample. GAI additive was added in the perovskite precursor for bulk passivation, as guanidinium ions introduced into the perovskite lattice form strong hydrogen bonds, enhancing thermal stability and preventing halide segregation.[30–32] Dark regions at the GBs of the perovskite persist, with current levels near 0 pA at the surface (Figure S5B). As the material is progressively removed, the extent of high-resistance regions rapidly decreases, which can be attributed to the effective bulk passivation engineering. The conductivity at the GBs also increases relative to that in the grains themselves, suggesting that the GAI treatment has facilitated carrier transport through the GBs. Figure 2C shows the current change of the perovskite film with PEAI post treatment, which also reduces the volume of high-resistance regions. Previous studies have suggested that PEAI post treatment on perovskite materials helps reduce iodine vacancies on the surface.[33–35] This modification reduces surface defects, thereby suppressing charge recombination and diminishing hysteresis, resulting in an increased open-circuit voltage (V_{OC}). Due to its insulating properties, and because PEAI tends to accumulate at GBs,[20] lower currents are observed on the surface and at the GBs (Figure S5C). As shown in Figure S6G and Table S1, after PEAI treatment, the sample surface shows the highest proportion of high-resistance regions among the four samples. However, once a small amount of material is removed in the near-surface region, the current value increases significantly (Figure S9). This indicates that the low conductivity at the film surface is due to the accumulation of PEAI rather than to high-resistance regions within the perovskite material. After removing the surface passivation material, the lateral distribution of high-resistance regions diminished, with only small amounts remaining near GBs (up to 25% depth). The dark regions disappear entirely at depths greater than 50%. These observations suggest that, although PEAI passivation is a surface treatment, it also penetrates the perovskite material.[36] The perovskite film treated with combined GAI and PEAI passivation exhibits the highest conductivity (Figure 2D), and due to the presence of high-resistance PEAI material, the dark regions are confined to the film's top surface. However, the high-resistance layers only persist for a few scans, and the overall conductivity is higher than that in untreated or individually passivated samples.

3D visualization of vertical conductivity and defect evolution

The 3D current volume further reveals the correlation and variation between these films, and we sliced different regions for cross-sectional analysis. Figure 3A shows high-resistance regions in the vertical direction within the untreated perovskite film. Different regions exhibit significant conductivity inhomogeneity from 0% to 70% depth. These high-resistance areas are randomly distributed around the surface GBs and extend inward, with the maximum depth of extension reaching approximately 450 nm. Despite a relatively uniform current distribution at the bottom of the film, the presence of these high-resistance regions along the vertical direction limits effective carrier transport. The high-resistance regions within the untreated perovskite exhibit various shapes. Area 1-1 shows a high-resistance region branching into a "Y"-shaped dark area. Area 1–2 indicates that the high-resistance region can grow along the GBs, as marked by the blue dashed line. Area 1–3 demonstrates that high-resistance regions on both sides of the grain may converge at the surface. These highlight the internal variability in conductivity, suggesting that the actual distribution of high-resistance regions within the material may be far more complex than what is seen on a surface scan. The distribution of these regions is likely influenced by nucleation and grain growth during film preparation, which contributes to the subpar performance of untreated films.

With bulk passivation, the current distribution is more uniform with a reduction in the depth of the high-resistance regions (Figure 3B). The high-resistance regions within the film after bulk passivation are located exclusively at the GBs on the film's top surface. Compared to untreated perovskite films, the dark localized regions in the bulk-passivated perovskite film are only confined to the upper 25% of the film. The volume and number of high-resistance regions are significantly reduced, and the types of these regions are becoming more limited, indicating a decrease in recombination centers within the perovskite film. In Areas 2-1 and 2-2, the grain interiors show uniform conductivity after bulk passivation, and highly conductive GBs in the vertical direction are visible, indicating improved charge transport properties. We measure depth-resolved current variations in two grains from each sample. The derivative analysis shows that GAI treatment significantly reduces the current fluctuations within the grains (Figure S10F). In contrast, the current at the GBs increases by 152%–265%, much higher than the 40%–128% observed in the untreated sample (Figures S11, S12, and Table S2). These results reveal that reducing high-resistance regions and improving GB conductivity effectively enable the GAI additive to enhance the electrical properties of perovskite materials. In Figure 3C, the cross-sectional results of the current volume further confirm the high-resistance surface and the penetration of PEAI along GBs. In areas 3-1, 3-2, and 3-3, small high-resistance regions and variations in grain conductivity are observed. Compared with the current within the grains, the GBs current is enhanced by 147%–210% (Table S2; Figure S13). The brighter regions represent higher conductivity, and uniform conductivity is observed across the vertical direction within the grains (Figures S10H and S10I), suggesting that PEAI has infiltrated through the GBs. Finally, for the film with combined GAI and PEAI treatment, the high-resistance regions are minimal and primarily located at the top surface. Although the vertical current is not uniform (Figures S10K and S10I), the higher current indicates improved longitudinal carrier transport (Figures 3D and S8G). Highly conductive GBs also provide pathways for vertical carrier transport (Table S2; Figure S14). The minimal presence of the high-resistance regions indicates a significant reduction in defect density throughout the film.

The TC-AFM results show that passivation treatment can effectively improve the film quality, with combined passivation

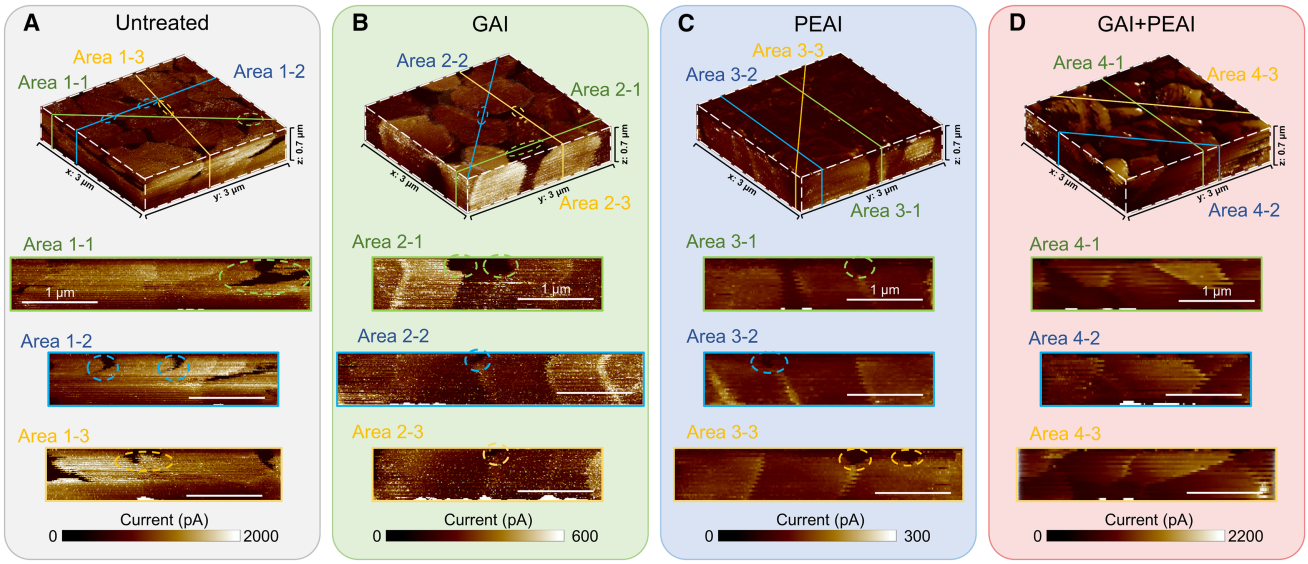

Figure 3. 3D current reconstruction and cross-sectional slices of perovskite samples

The gray, green, blue, and red boxes show the 3D current volumes of the (A) untreated, (B) GAI-treated, (C) PEAI-treated, and (D) GAI+PEAI-treated samples. Current cross-sections were extracted along the green, blue, and yellow lines marked within each 3D volume, representing three distinct regions of interest. The dashed circles indicate high-resistance regions identified in the samples.

treatment offering better suppression of high-resistance regions and enhanced film conductivity compared to individual passivation treatments. The most noticeable change in the high-conductivity regions across different passivated samples is observed here. After individual passivation, the high-resistance regions decrease and are confined to the GBs. However, we did not detect obvious high-resistance areas after the combined passivation treatment. Additionally, the vertical current becomes more uniform following individual passivation, facilitating smoother vertical carrier transport. The overall current value of the combined passivated sample is higher than that of the individually passivated samples, indicating superior conductivity. Since GBs and defects in polycrystalline films inevitably affect carrier transport, reduced high-resistance regions and improved conductivity within the perovskite material promote carrier transport and reduce non-radiative recombination. Furthermore, the lower conductivity at the top surface contributes to the smaller leakage current across the interface between the perovskite and the following carrier-transport layer. These findings highlight the importance of passivation treatments in optimizing the performance of perovskite materials for electronic applications.

Correlation with crystallinity, ultrafast carrier dynamics, and device performance

X-ray diffraction (XRD) analysis (Figure S15) was performed to assess the crystallinity of perovskite films with different passivation treatments. Distinct characteristic peaks around 14° and 28.2°, corresponding to the (100) and (200) planes,[37–39] are more pronounced in the passivated samples (Table S3), indicating enhanced crystallinity and the absence of new phase formation. These results indicate that effective passivation treatments improve the crystallinity of perovskite films and help suppress defect formation. Further, grazing incidence XRD (GIXRD) was employed to investigate the residual stress in the films. Diffraction patterns were obtained at 0.1°, 0.5°, 0.7°, and 1.0°, where higher incident angles allow for the detection of stress in the deeper region of the film,[40,41] and characteristic peaks at larger diffraction angles were selected for analysis[42] (Figure S16). We find that the diffraction peaks gradually shift to lower angles as the grazing incidence angle increases from 0.1° to 1°. According to Bragg's law, this shift indicates an increase in interplanar spacing, which suggests that greater tensile stress exists in the untreated perovskite film.[43] After passivation, this peak shift was significantly reduced, indicating a release of internal tensile stress. This reduction can be attributed to the effective defect passivation provided by GAI and PEAI, which alleviates the internal residual stress in the perovskite film. These findings are consistent with TC-AFM results, confirming the passivation effects on the material's internal structure.

Transient reflection (TR) spectroscopy was employed to investigate the effects of PEAI surface passivation and GAI bulk passivation on carrier recombination dynamics.[44–47] Figure 4A illustrates the processes of photoexcited carrier diffusion, surface recombination, and bulk recombination within the film. The Kramers-Kronig (K-K) transform was used to correlate transient absorption (TA) and TR spectra, deriving ideal TR spectra from experimentally measured TA spectra at low carrier densities (Table S4). The well-overlapped TR spectrum and the K-K transform of the TA spectrum confirm that the TR signal from 700 to 770 nm originated from relaxed carriers (Figure S17). The rapid decay observed in the TR dynamics is mainly due to carrier diffusion and surface recombination.

To quantify the two key parameters—the diffusion coefficient (D) and surface recombination rate (S)—TR measurements were performed on the four perovskite films using different pump photon energies (Figures 4B–4E and S18). The carrier

Please cite this article in press as: Li et al., Three-dimensional mapping of electrical behavior in perovskite films using tomographic conductive atomic force microscopy, Newton (2025), https://doi.org/10.1016/j.newton.2025.100367

dynamics were modeled and globally fitted using the following equations[46,47]:

$$\frac{\partial N(x,t)}{\partial t} = D\frac{\partial^2 N(x,t)}{\partial x^2} - \frac{N(x,t)}{\tau_B} \quad \text{(Equation 1)}$$

$$N(x,t)|_{t=0} = N_0 e^{-\alpha x} \quad \text{(Equation 2)}$$

$$\left.\frac{\partial N(x,t)}{\partial t}\right|_{x=0} = \frac{S}{D}N(0,t) \quad \text{(Equation 3)}$$

$$\left.\frac{\partial N(x,t)}{\partial t}\right|_{x=L_{PC}} = -\frac{S}{D}N(L_{PC},t), \quad \text{(Equation 4)}$$

where N (x, t) is the carrier concentration, D is the diffusion coefficient, τ_B is the bulk carrier lifetime, N_0 is the initial surface carrier concentration, α is the absorption coefficient of the film at the selected photon energy, L_{PC} is the film thickness from cross-sectional scanning electron microscopy (Figure S19), and S is the surface recombination velocity. Because the bulk carrier recombination of the perovskite film is negligible within the 1-ns delay range, the bulk recombination term in Equation 1 is omitted. By varying the pump photon energy and consequently adjusting α in the initial condition (Equation 2), the solid lines in Figures 4B–4E were fitted. Figure S20 shows the carrier dynamics within the 10-ps timescale. A faster decay at higher photon energies was observed, which can be attributed to the steeper gradient of the initial photogenerated carrier distribution.

The extracted fitting parameters are summarized in Table S5, and the detailed analysis method is in the supplemental information. For the untreated film, D is 1.16 cm^2/s, and S is 660 cm/s, which agree well with typical values for a 3D perovskite polycrystalline thin film.[46] After GAI bulk passivation, D increases to 1.38 cm^2/s, and S decreases to 550 cm/s, indicating enhanced charge transport and reduced recombination. Surface passivation with PEAI further improved the film quality, with D similar to the untreated film but S decreasing significantly to 330 cm/s. Notably, when both GAI bulk passivation and PEAI surface passivation were applied, the perovskite film exhibits the best performance, achieving a D of 1.35 cm^2/s and an S of 230 cm/s. These results demonstrate that the combination of bulk and surface passivation yields the highest carrier diffusion rate and the lowest surface recombination rate, highlighting the effectiveness of the dual passivation strategy in enhancing carrier transport in perovskite films.

To confirm the passivation effect on device performance, we fabricated corresponding devices. For p-i-n devices, the statistical power conversion efficiency (PCE) increases from approximately 23.3% in the untreated device to 24.5%, 24.7%, and 25.1% following bulk, surface, and combined passivation treatments, respectively (Figure S21; representative current-voltage (J-V) curves and photovoltaic parameters are shown in Figure S22). The improvement from surface passivation with PEAI is attributed to reduced surface defects and the suppression of interfacial charge recombination. In contrast, bulk passivation with GAI enhances crystallinity and suppresses recombination within the perovskite layer, thereby improving charge transport. These effects are reflected in the V_{OC}; surface and bulk passivation raised V_{OC} from 1.13 V to 1.15 V. The combination of both treatments resulted in the highest efficiency, alongside an increase in fill factor (FF), consistent with the TC-AFM results. To better illustrate the differences among the three passivation strategies, p-i-n devices were fabricated with $FA_{0.8}MA_{0.15}Cs_{0.05}PbI_3$. The n-i-p devices based on $FAPbI_3$, the same composition as used in the TC-AFM experiments, show similar trends (Figure S23). These results highlight the broad applicability of the passivation treatments.

Electrochemical impedance spectroscopy (EIS) data (Figure S24 and Table S6) show a clear increase in recombination resistance (R_{rec}) with passivation. The combined passivation treatment raised R_{rec} from 460.44 to 664.25 Ω, while series resistance (R_s) remained nearly unchanged. This suggests improved charge extraction and reduced recombination losses.[48] The Mott-Schottky analysis in Figure S25 shows that passivation also increases the built-in potential (V_{bi}), thereby improving charge separation.[49] Space-charge-limited current (SCLC) measurements were used to estimate trap densities with the hole-only device structure (Figure S26). The trap densities calculated using the previous formula[50] are 12.53×10^{15}, 9.66×10^{15}, 8.49×10^{15}, and 5.73×10^{15} cm^{-3} for the untreated, bulk, surface, and combined passivated devices, respectively. These reductions reflect fewer defect-induced recombination centers, consistent with the observed electrical improvements.

Finally, stability tests demonstrate that passivation also enhances environmental resilience. After 400 h of storage under ambient conditions, the untreated device retains only 55% of its original efficiency, while the combined passivated device maintains 86%. Devices with only bulk or surface passivation retain 74% and 81% of their initial PCE, respectively (Figure S27). Overall, passivation engineering, particularly the combined use of surface and bulk treatments, enhances charge transport, suppresses non-radiative recombination, and significantly improves long-term device stability. The 3D TC-AFM measurements reveal how these improvements correlate with reduced internal resistance and more uniform conductivity, highlighting the technique's potential for in-depth material diagnostics.

DISCUSSION

In summary, this study highlights the powerful role of 3D TC-AFM in providing detailed insights into the impact of passivation on perovskite materials and devices. By combining TC-AFM with other characterization techniques, we could closely examine how surface and bulk passivation treatments affect the local electrical properties, crystallinity, and charge transport within perovskite films. Our results demonstrate that passivation significantly improves the material quality by reducing recombination centers, enhancing crystallinity, and suppressing non-radiative recombination. This leads to substantial improvements in device performance, with the combined passivation treatment achieving the highest PCE, V_{OC}, and FF. Notably, the ability of passivation treatments to improve both the electrical characteristics at the film surface and bulk material properties underscores their critical role in optimizing PSC performance. The enhanced stability observed

Please cite this article in press as: Li et al., Three-dimensional mapping of electrical behavior in perovskite films using tomographic conductive atomic force microscopy, Newton (2025), https://doi.org/10.1016/j.newton.2025.100367

CellPress
OPEN ACCESS

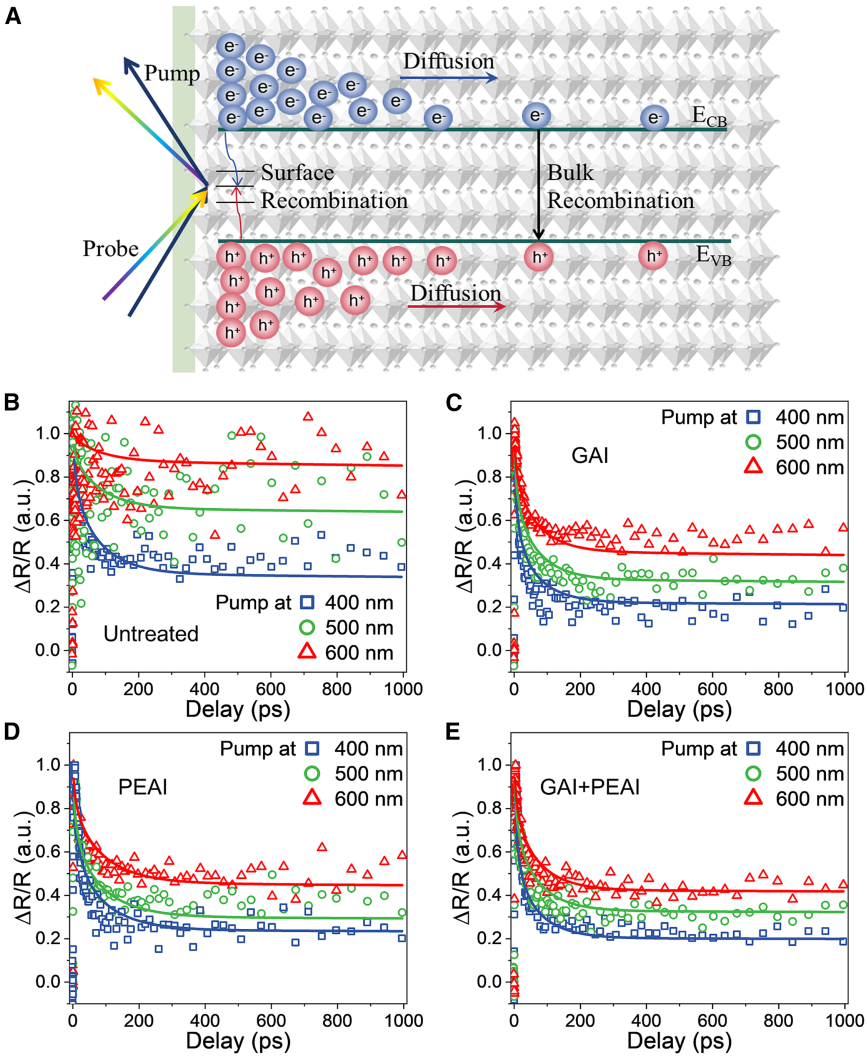

Figure 4. Ultrafast TR spectra of perovskite films

(A) Schematic of the TR setup, where an ultrafast pump pulse excites carriers near the perovskite surface, and a delayed broadband probe monitors the resulting changes in reflectivity to track carrier dynamics.

(B-E) Normalized TR kinetics and global fitting results for the untreated (B), GAI-treated (C), PEAI-treated (D), and GAI+PEAI-treated (E) films. Three pump wavelengths (400, 500, and 600 nm) were used to generate different photocarrier density gradients, enabling global fitting of the one-dimensional diffusion equation to obtain the surface recombination velocity (S) and carrier diffusion coefficient (D). The solid lines represent the corresponding global fits.

with passivated devices further emphasizes the potential of passivation engineering to address long-term operational challenges in perovskite photovoltaics. Overall, this work reinforces the effectiveness of passivation treatments and demonstrates the utility of 3D TC-AFM as a valuable tool for understanding the fundamental processes that govern the performance of advanced perovskite materials and devices.

METHODS

Materials

All chemical reagents were used as received without further purification. Formamidinium iodide (FAI; 99.5%), lead iodide (PbI_2; 99.99%), and fluorine-doped tin oxide (FTO) and ITO were purchased from Yingkou Advanced Election Technology. N,N-dimethylformamide (DMF; 99.8%), dimethyl sulfoxide (DMSO; 99.8%), isopropanol (IPA; 99.5%), and chlorobenzene (CB; 99.9%) were obtained from Sigma-Aldrich. 4-*tert*-butyl pyridine (tBP; 96%), lithium bis(trifluoromethanesulfonyl)imide (LiTFSI), 2,2′,7,7′-tetrakis-(N,N,di-p-methoxyphenylamine)-9,9′-spirobifluorene (spiro-OMeTAD; 99.5%), GAI (99.5%), and PEAI (99.5%) were purchased from Xi'an Polymer Light Technology (China). SnO_2 colloidal solution (15 wt % in H_2O) was purchased from Alfa Aesar.

Device fabrication

The n-i-p and p-i-n device structures were glass/FTO/SnO_2/$FAPbI_3$/spiro-OMeTAD/Ag and ITO/2PACz/$FA_{0.8}MA_{0.15}Cs_{0.05}PbI_3$/LiF/$C_{60}$/BCP/Ag, respectively, following Liu et al.[51] For the $FAPbI_3$ perovskite, a solution was prepared by dissolving a specific concentration of FAI and PbI_2 in a mixed solvent of DMF and DMSO (4:1 ratio). The mixture was stirred and shaken for 4–5 h to ensure homogeneity. The perovskite solution was spin coated at 5,000 rpm for 30 s, with 200 μL CB added as an antisolvent during the spin coating. The film was then annealed at 150°C for 10 min.

For the $FA_{0.8}MA_{0.15}Cs_{0.05}PbI_3$ perovskite precursor (1.5 M), FAI, CsI, MABr, MAI, and PbI_2 were dissolved in a mixed solvent of anhydrous DMF and DMSO (4:1 [v/v]) with the appropriate stoichiometry. The perovskite precursor (60 μL) was spin coated onto the SAMs/ITO substrate at 1,000 rpm for 10 s, followed by 5,000 rpm for 30 s. The film was then annealed at 100°C for 45 min to complete the perovskite film formation.

For bulk passivation samples, 1 mg of GAI was added to the precursor solution. For surface passivation samples, PEAI was prepared at a 1.25 mg/mL concentration in IPA and spin-coated at 5,000 rpm for 25 s.

C-AFM

The C-AFM measurements were performed on a Bruker Icon atomic force microscope inside an argon-filled glovebox with oxygen and water levels lower than 1 ppm. The scanning probe was a DDESP-V2 conductive probe coated with conductive

doped diamond material to enhance wear resistance and conductivity. The probe has a high elastic constant (k) of approximately 80 N/m, enabling a greater force to be applied to the sample. The current sensitivity was set to 2 nA/V, and the current measurement range is 0–25 nA. A constant bias voltage of 900 mV was applied to the samples. The scan image size and the number of scan lines were optimized to ensure the average scan line width remained smaller than the probe tip's actual diameter. Initially, a lower force was applied to avoid wearing the sample surface. After recording topography images and the current state of the sample surface, the set point was adjusted to a higher force for material removal. Throughout the layer-by-layer analysis, we maintained consistent parameters to ensure a uniform milling rate across consecutive current images. The TC-AFM samples had the structure glass/ITO/$FAPbI_3$, with passivation treatments as described above.

TA and TR measurements

TA and TR measurements are conducted using a pump-probe spectrometer setup in transmission and reflection mode, respectively. Initially, a Ti:sapphire amplifier generates a fundamental laser pulse at 800 nm, operating at a 1 kHz repetition rate. This fundamental pulse is then split into two branches by a beam splitter. One branch is directed toward an optical parametric amplifier to generate the pump pulse from 290 to 2600 nm. The pump pulse, modulated at 500 Hz, is attenuated by neutral-density filter wheels. Simultaneously, the other branch of the fundamental pulse is focused into a sapphire crystal to produce a white-light continuum spanning 350–1600 nm, which is used as the probe. Time delays between the pump and probe pulses (up to 8 ns) are achieved using a motorized translation stage with a retro-reflecting mirror. The pump and probe beams are spatially overlapped on the sample surface. In the TA configuration, both beams are usually incident on the sample. In the TR configuration, the probe beam incident angle is fixed at 45°, while the pump beam incident on the sample normally. The focused spot size at the sample position is approximately 200 μm for the probe beam and 600 μm for the pump beam.

Other measurements and characterizations

XRD patterns were collected by Mini Flex 600 with a Cu-Kα1 X-ray source. Scanning electron microscope (SEM) images were collected using a Hitachi S-4800 field emission gun SEM. EIS and Mott-Schottky curves were obtained using an electrochemical workstation (model 600E). The out-plane mobilities were measured using the SCLC method.[52] PSCs were placed under the AM1.5 solar simulator (100 mW cm^{-2}). The Keithley 2400 source meter was used to test and record J-V curves at a scan rate of 100 mV s^{-1} with an effective area of 0.12 cm^2. All measurements were performed at room temperature and <40% humidity.

RESOURCE AVAILABILITY

Lead contact

Requests for further information and resources should be directed to and will be fulfilled by the lead contact, Chuanxiao Xiao (cxiao@nimte.ac.cn).

Materials availability

This study did not generate new unique materials.

Data and code availability

The raw data that support the findings of this study are available from the corresponding author upon request.

ACKNOWLEDGMENTS

This work was supported by the Ningbo Institute of Materials Technology & Engineering (NIMTE), a research institute of the Chinese Academy of Sciences (CAS). C.X. is thankful for support from the National Natural Science Foundation of China (52302327), the International Cooperation Project of CAS (181GJHZ2024122MI and 181GJHZ2024092FN), and the International Cooperation Project of Ningbo City (2024H034). Y. Zhai is thankful for financial support from the National Natural Science Foundation of China (NSFC) (grants 62522404 and 12421005), the Science & Technology Department (grants 2024JJ2041 and 2023ZJ1010), and the Education Department of Hunan Province (grant 23A0047). F.Z. is thankful for financial support from the Key Fund Project of Tianjin Natural Science Foundation (24JCZDJC00510), the National Natural Science Foundation of China (22475147), and the Fundamental Research Funds for the Central Universities.

AUTHOR CONTRIBUTIONS

M.L. and C.X. conceived ideas, designed experiments, and performed the main data analysis. M.L. was responsible for the tomographic C-AFM tests of different samples. P.W. and Y.S. prepared the samples and characterized J-V curves, Nyquist plots, Mott-Schottky curves, and SCLC. P.W. assisted M.L. in analyzing the characterization data. J.L., and Y. Zhai conducted the TR spectra characterization measurements. H.T. and Y.G. performed the cross-sectional SEM measurements. X. Lang and Y. Zhang assisted M.L. in data organization and figure preparation. Z.Y., X. Liu, and Y.J. participated in the discussions regarding data analysis. M.L. wrote the initial manuscript draft. F.Z. and C.X. revised and finalized the manuscript. J.Y., Y. Zhai, F.Z., and C.X. supervised the project, and all of the authors contributed to the revision and discussion of the results.

DECLARATION OF INTERESTS

The authors declare no competing interests.

SUPPLEMENTAL INFORMATION

Supplemental information can be found online at https://doi.org/10.1016/j.newton.2025.100367.

Received: June 10, 2025
Revised: October 15, 2025
Accepted: December 9, 2025

REFERENCES

1. Ju, D., Dang, Y., Zhu, Z., Liu, H., Chueh, C.-C., Li, X., Wang, L., Hu, X., Jen, A.K.-Y., and Tao, X. (2018). Tunable band gap and long carrier recombination lifetime of stable mixed $CH_3NH_3Pb_xSn_{1-x}Br_3$ single crystals. Chem. Mater. *30*, 1556–1565. https://doi.org/10.1021/acs.chemmater.7b04565.
2. Zhao, D., Yu, Y., Wang, C., Liao, W., Shrestha, N., Grice, C.R., Cimaroli, A.J., Guan, L., Ellingson, R.J., Zhu, K., et al. (2017). Low-bandgap mixed tin–lead iodide perovskite absorbers with long carrier lifetimes for all-perovskite tandem solar cells. Nat. Energy *2*, 17018. https://doi.org/10.1038/nenergy.2017.18.
3. Yang, Z., Yu, Z., Wei, H., Xiao, X., Ni, Z., Chen, B., Deng, Y., Habisreutinger, S.N., Chen, X., Wang, K., et al. (2019). Enhancing electron diffusion length in narrow-bandgap perovskites for efficient monolithic perovskite

Please cite this article in press as: Li et al., Three-dimensional mapping of electrical behavior in perovskite films using tomographic conductive atomic force microscopy, Newton (2025), https://doi.org/10.1016/j.newton.2025.100367

tandem solar cells. Nat. Commun. *10*, 4498. https://doi.org/10.1038/s41467-019-12513-x.

4. Xu, F., Zhang, M., Li, Z., Yang, X., and Zhu, R. (2023). Challenges and perspectives toward future wide-bandgap mixed-halide perovskite photovoltaics. Adv. Energy Mater. *13*, 2203911. https://doi.org/10.1002/aenm.202203911.
5. Park, J., Kim, J., Yun, H.-S., Paik, M.J., Noh, E., Mun, H.J., Kim, M.G., Shin, T.J., and Seok, S.I. (2023). Controlled growth of perovskite layers with volatile alkylammonium chlorides. Nature *616*, 724–730. https://doi.org/10.1038/s41586-023-05825-y.
6. Fu, Q., and Jen, A.K.Y. (2023). Perovskite solar cell developments, what's next? Next Energy *1*, 100004. https://doi.org/10.1016/j.nxener.2023.100004.
7. Lei, Y., Xu, Y., Wang, M., Zhu, G., and Jin, Z. (2021). Origin, influence, and countermeasures of defects in perovskite solar cells. Small *17*, 2005495. https://doi.org/10.1002/smll.202005495.
8. Zhang, H., Cheng, J., Li, D., Lin, F., Mao, J., Liang, C., Jen, A.K.-Y., Grätzel, M., and Choy, W.C.H. (2017). Toward all room-temperature, solution-processed, high-performance planar perovskite solar cells: a new scheme of pyridine-promoted perovskite formation. Adv. Mater. *29*, 1604695. https://doi.org/10.1002/adma.201604695.
9. Isikgor, F.H., Zhumagali, S., T. Merino, L.V., De Bastiani, M., McCulloch, I., and De Wolf, S. (2022). Molecular engineering of contact interfaces for high-performance perovskite solar cells. Nat. Rev. Mater. *8*, 89–108. https://doi.org/10.1038/s41578-022-00503-3.
10. Frohna, K., Chosy, C., Al-Ashouri, A., Scheler, F., Chiang, Y.-H., Dubajic, M., Parker, J.E., Walker, J.M., Zimmermann, L., Selby, T.A., et al. (2025). The impact of interfacial quality and nanoscale performance disorder on the stability of alloyed perovskite solar cells. Nat. Energy *10*, 66–76. https://doi.org/10.1038/s41560-024-01660-1.
11. Li, C., Wang, X., Bi, E., Jiang, F., Park, S.M., Li, Y., Chen, L., Wang, Z., Zeng, L., Chen, H., et al. (2023). Rational design of Lewis base molecules for stable and efficient inverted perovskite solar cells. Science *379*, 690–694. https://doi.org/10.1126/science.ade3970.
12. Liu, C., Yang, Y., Chen, H., Xu, J., Liu, A., Bati, A.S.R., Zhu, H., Grater, L., Hadke, S.S., Huang, C., et al. (2023). Bimolecularly passivated interface enables efficient and stable inverted perovskite solar cells. Science *382*, 810–815. https://doi.org/10.1126/science.adk1633.
13. Yang, Y., Chen, H., Liu, C., Xu, J., Huang, C., Malliakas, C.D., Wan, H., Bati, A.S.R., Wang, Z., Reynolds, R.P., et al. (2024). Amidination of ligands for chemical and field-effect passivation stabilizes perovskite solar cells. Science *386*, 898–902. https://doi.org/10.1126/science.adr2091.
14. Degani, M., An, Q., Albaladejo-Siguan, M., Hofstetter, Y.,J., Cho, C., Paulus, F., Grancini, G., and Y, V. (2021). 23.7% efficient inverted perovskite solar cells by dual interfacial modification. Sci. Adv. *7*, eabj7930. https://doi.org/10.1126/sciadv.abj7930.
15. Liu, X., Yu, Z., Wang, T., Chiu, K.L., Lin, F., Gong, H., Ding, L., and Cheng, Y. (2020). Full defects passivation enables 21% efficiency perovskite solar cells operating in air. Adv. Energy Mater. *10*, 2001958. https://doi.org/10.1002/aenm.202001958.
16. Zhou, X., Luan, X., Zhang, L., Hu, H., Jiang, Z., Li, Y., Wu, J., Liu, Y., Chen, J., Wang, D., et al. (2023). Dual optimization of bulk and interface via the synergistic effect of ligand anchoring and hole transport dopant enables 23.28% efficiency inverted perovskite solar cells. ACS Nano *17*, 3776–3785. https://doi.org/10.1021/acsnano.2c11615.
17. Zheng, Y., Tian, C., Wu, X., Sun, A., Zhuang, R., Tang, C., Liu, Y., Li, Z., Ouyang, B., Du, J., et al. (2024). Dual-interface modification for inverted methylammonium-free perovskite solar cells of 25.35% efficiency with balanced crystallization. Adv. Energy Mater. *14*, 2304486. https://doi.org/10.1002/aenm.202304486.
18. Zhou, S., Fu, S., Wang, C., Meng, W., Zhou, J., Zou, Y., Lin, Q., Huang, L., Zhang, W., Zeng, G., et al. (2023). Aspartate all-in-one doping strategy enables efficient all-perovskite tandems. Nature *624*, 69–73. https://doi.org/10.1038/s41586-023-06707-z.
19. Luria, J., Kutes, Y., Moore, A., Zhang, L., Stach, E.A., and Huey, B.D. (2016). Charge transport in CdTe solar cells revealed by conductive tomographic atomic force microscopy. Nat. Energy *1*, 16150. https://doi.org/10.1038/nenergy.2016.150.
20. Stetson, C., Yoon, T., Coyle, J., Nemeth, W., Young, M., Norman, A., Pylypenko, S., Ban, C., Jiang, C.-S., Al-Jassim, M., and Burrell, A. (2019). Three-dimensional electronic resistivity mapping of solid electrolyte interphase on Si anode materials. Nano Energy *55*, 477–485. https://doi.org/10.1016/j.nanoen.2018.11.007.
21. Stetson, C., Huey, Z., Downard, A., Li, Z., To, B., Zakutayev, A., Jiang, C.-S., Al-Jassim, M.M., Finegan, D.P., Han, S.-D., and DeCaluwe, S.C. (2020). Three-dimensional mapping of resistivity and microstructure of composite electrodes for lithium-ion batteries. Nano Lett. *20*, 8081–8088. https://doi.org/10.1021/acs.nanolett.0c03074.
22. Song, J., Zhou, Y., Padture, N.P., and Huey, B.D. (2020). Anomalous 3D nanoscale photoconduction in hybrid perovskite semiconductors revealed by tomographic atomic force microscopy. Nat. Commun. *11*, 3308. https://doi.org/10.1038/s41467-020-17012-y.
23. Sharma, D., Nicoara, N., Jackson, P., Witte, W., Hariskos, D., and Sadewasser, S. (2024). Charge-carrier-concentration inhomogeneities in alkali-treated Cu(In,Ga)Se_2 revealed by conductive atomic force microscopy tomography. Nat. Energy *9*, 163–171. https://doi.org/10.1038/s41560-023-01420-7.
24. Jiang, Q., Tong, J., Xian, Y., Kerner, R.A., Dunfield, S.P., Xiao, C., Scheidt, R.A., Kuciauskas, D., Wang, X., Hautzinger, M.P., et al. (2022). Surface reaction for efficient and stable inverted perovskite solar cells. Nature *611*, 278–283. https://doi.org/10.1038/s41586-022-05268-x.
25. Noël, C., Wouters, L., Paredis, K., Celano, U., and Hantschel, T. (2021). Oil as an enabler for efficient materials removal in three-dimensional scanning probe microscopy applications. Front. Mech. Eng. *7*, 797962. https://doi.org/10.3389/fmech.2021.797962.
26. Laskar, M.A.R., Leonetti, G., Milano, G., Novotný, O., Neuman, J., Tongay, S., and Celano, U. (2024). Adaptive scalpel scanning probe microscopy for enhanced volumetric sensing in tomographic analysis. Adv Materials Inter *11*, 2400187. https://doi.org/10.1002/admi.202400187.
27. Liu, X., Lu, X., Lang, X., Li, M., Gou, Y., Jiang, Y., Zhang, J., Tian, H., Zhang, Y., Xi, H., et al. (2025). Direct measurement of carrier distribution in perovskite by scanning capacitance microscopy. J. Phys. Chem. C *129*, 648–657. https://doi.org/10.1021/acs.jpcc.4c06178.
28. Rijal, S., Li, D., Awni, R.A., Xiao, C., Bista, S.S., Jamarkattel, M.K., Heben, M.J., Jiang, C., Al-Jassim, M., Song, Z., and Yan, Y. (2022). Templated growth and passivation of vertically oriented antimony selenide thin films for high-efficiency solar cells in substrate configuration. Adv. Funct. Mater. *32*, 2110032. https://doi.org/10.1002/adfm.202110032.
29. Du, L., Cao, F., Meng, R., Zhang, Y., Zhang, J., Gao, Z., Chen, C., Li, C., Zhao, D., Ye, J., et al. (2025). Photo-homogenization assisted segregation easing technique (PHASET) for highly efficient and stable wide-bandgap perovskite solar cells. Nat. Commun. *16*, 8080. https://doi.org/10.1038/s41467-025-63176-w.
30. Jokar, E., Chien, C.H., Tsai, C.M., Fathi, A., and Diau, E.W.G. (2019). Robust tin-based perovskite solar cells with hybrid organic cations to attain efficiency approaching 10%. Adv. Mater. *31*, 1804835. https://doi.org/10.1002/adma.201804835.
31. Yao, Q., Xue, Q., Li, Z., Zhang, K., Zhang, T., Li, N., Yang, S., Brabec, C.J., Yip, H.L., and Cao, Y. (2020). Graded 2D/3D perovskite heterostructure for efficient and operationally stable MA-free perovskite solar cells. Adv. Mater. *32*, 2000571. https://doi.org/10.1002/adma.202000571.
32. Zhou, Y., Xue, H., Jia, Y., Brocks, G., Tao, S., and Zhao, N. (2019). Enhanced incorporation of guanidinium in formamidinium-based perovskites for efficient and stable photovoltaics: the role of Cs and Br. Adv. Funct. Mater. *29*, 1905739. https://doi.org/10.1002/adfm.201905739.

Please cite this article in press as: Li et al., Three-dimensional mapping of electrical behavior in perovskite films using tomographic conductive atomic force microscopy, Newton (2025), https://doi.org/10.1016/j.newton.2025.100367

33. Liu, Z., Zhu, C., Luo, H., Kong, W., Luo, X., Wu, J., Ding, C., Chen, Y., Wang, Y., Wen, J., et al. (2023). Grain regrowth and bifacial passivation for high-efficiency wide-bandgap perovskite solar cells. Adv. Energy Mater. *13*, 2203230. https://doi.org/10.1002/aenm.202203230.

34. Kim, D., Jung, H.J., Park, I.J., Larson, B.W., Dunfield, S.P., Xiao, C., Kim, J., Tong, J., Boonmongkolras, P., Ji, S.G., et al. (2020). Efficient, stable silicon tandem cells enabled by anion-engineered wide-bandgap perovskites. Science *368*, 155–160. https://doi.org/10.1126/science.aba3433.

35. Jiang, Q., Zhao, Y., Zhang, X., Yang, X., Chen, Y., Chu, Z., Ye, Q., Li, X., Yin, Z., and You, J. (2019). Surface passivation of perovskite film for efficient solar cells. Nat. Photon. *13*, 460–466. https://doi.org/10.1038/s41566-019-0398-2.

36. Chen, C., Song, Z., Xiao, C., Awni, R.A., Yao, C., Shrestha, N., Li, C., Bista, S.S., Zhang, Y., Chen, L., et al. (2020). Arylammonium-assisted reduction of the open-circuit voltage deficit in wide-bandgap perovskite solar cells: the role of suppressed ion migration. ACS Energy Lett. *5*, 2560–2568. https://doi.org/10.1021/acsenergylett.0c01350.

37. Huang, Z., Bai, Y., Huang, X., Li, J., Wu, Y., Chen, Y., Li, K., Niu, X., Li, N., Liu, G., et al. (2023). Anion–π interactions suppress phase impurities in $FAPbI_3$ solar cells. Nature *623*, 531–537. https://doi.org/10.1038/s41586-023-06637-w.

38. Wang, S., Miao, Z., Yang, J., Gu, Z., Li, P., Zhang, Y., and Song, Y. (2024). Lead-chelating intermediate for air-processed phase-pure $FAPbI_3$ perovskite solar cells. Angew. Chem. Int. Ed. *63*, e202407192. https://doi.org/10.1002/anie.202407192.

39. Yang, T., Yang, Y., Niu, T., Zhao, E., Wu, N., Wang, S., Chen, X., Wang, S., Wang, Y., Wu, Y., et al. (2025). Facet orientation-dependent strain relaxation stabilizes $FAPbI_3$ perovskite solar cells. ACS Energy Lett. *10*, 427–438. https://doi.org/10.1021/acsenergylett.4c02674.

40. Zhu, C., Niu, X., Fu, Y., Li, N., Hu, C., Chen, Y., He, X., Na, G., Liu, P., Zai, H., et al. (2019). Strain engineering in perovskite solar cells and its impacts on carrier dynamics. Nat. Commun. *10*, 815. https://doi.org/10.1038/s41467-019-08507-4.

41. Wang, H., Zhu, C., Liu, L., Ma, S., Liu, P., Wu, J., Shi, C., Du, Q., Hao, Y., Xiang, S., et al. (2019). Interfacial residual stress relaxation in perovskite solar cells with improved stability. Adv. Mater. *31*, 1904408. https://doi.org/10.1002/adma.201904408.

42. Liu, B., Bi, H., He, D., Bai, L., Wang, W., Yuan, H., Song, Q., Su, P., Zang, Z., Zhou, T., and Chen, J. (2021). Interfacial defect passivation and stress release via multi-active-site ligand anchoring enables efficient and stable methylammonium-free perovskite solar cells. ACS Energy Lett. *6*, 2526–2538. https://doi.org/10.1021/acsenergylett.1c00794.

43. Liu, D., Luo, D., Iqbal, A.N., Orr, K.W.P., Doherty, T.A.S., Lu, Z.-H., Stranks, S.D., and Zhang, W. (2021). Strain analysis and engineering in halide perovskite photovoltaics. Nat. Mater. *20*, 1337–1346. https://doi.org/10.1038/s41563-021-01097-x.

44. Yang, Y., Yan, Y., Yang, M., Choi, S., Zhu, K., Luther, J.M., and Beard, M.C. (2015). Low surface recombination velocity in solution-grown $CH_3NH_3PbBr_3$ perovskite single crystal. Nat. Commun. *6*, 7961. https://doi.org/10.1038/ncomms8961.

45. Chen, X., Wang, K., and Beard, M.C. (2019). Ultrafast probes at the interfaces of solar energy conversion materials. Phys. Chem. Chem. Phys. *21*, 16399–16407. https://doi.org/10.1039/C9CP02768H.

46. Yang, Y., Yang, M., Moore, D.T., Yan, Y., Miller, E.M., Zhu, K., and Beard, M.C. (2017). Top and bottom surfaces limit carrier lifetime in lead iodide perovskite films. Nat. Energy *2*, 16207. https://doi.org/10.1038/nenergy.2016.207.

47. Xiao, C., Zhang, F., Chen, X., Yang, M., Harvey, S.P., Beard, M.C., Berry, J.J., Jiang, C.-S., Al-Jassim, M.M., and Zhu, K. (2021). SMART perovskite growth: enabling a larger range of process conditions. ACS Energy Lett. *6*, 650–658. https://doi.org/10.1021/acsenergylett.0c02578.

48. Chen, Y., Ying, Z., Li, X., Wang, X., Wu, J., Wu, M., Sun, J., Sheng, J., Zeng, Y., Yan, B., et al. (2022). Self-sacrifice alkali acetate seed layer for efficient four-terminal perovskite/silicon tandem solar cells. Nano Energy *100*, 107529. https://doi.org/10.1016/j.nanoen.2022.107529.

49. Wang, J., Jiao, B., Tian, R., Sun, K., Meng, Y., Bai, Y., Lu, X., Han, B., Yang, M., Wang, Y., et al. (2025). Less-acidic boric acid-functionalized self-assembled monolayer for mitigating NiO_x corrosion for efficient all-perovskite tandem solar cells. Nat. Commun. *16*, 4148. https://doi.org/10.1038/s41467-025-59515-6.

50. Niu, T., Lu, J., Munir, R., Li, J., Barrit, D., Zhang, X., Hu, H., Yang, Z., Amassian, A., Zhao, K., and Liu, S.F. (2018). Stable high-performance perovskite solar cells via grain boundary passivation. Adv. Mater. *30*, 1706576. https://doi.org/10.1002/adma.201706576.

51. Liu, H., Zhang, Z., Shi, Y., Ran, W., Zhong, H., and Zhang, F. (2025). A low-cost and bendable "cage" for stable rigid and flexible perovskite solar cells with negligible lead leakage. Joule *9*, 101816. https://doi.org/10.1016/j.joule.2024.101816.

52. Zhang, F., Park, S.Y., Yao, C., Lu, H., Dunfield, S.P., Xiao, C., Uličná, S., Zhao, X., Du Hill, L., Chen, X., et al. (2022). Metastable Dion-Jacobson 2D structure enables efficient and stable perovskite solar cells. Science *375*, 71–76. https://doi.org/10.1126/science.abj2637.

NEWTON, Volume *2*

Supplemental information

Three-dimensional mapping of electrical behavior in perovskite films using tomographic conductive atomic force microscopy

Minghui Li, Pengfei Wu, Jiali Liu, Xiting Lang, Yating Shi, Xirui Liu, Hao Tian, Yongjie Jiang, Yangyang Gou, Yueying Zhang, Zhenhai Yang, Jichun Ye, Yaxin Zhai, Fei Zhang, and Chuanxiao Xiao

Supplemental Information

This PDF file includes:

1. Supplemental Figures

2. Supplemental Tables

Table S5. Fitted diffusion coefficients and surface recombination rates for the untreated, GAI, PEAI, and GAI+PEAI-treated perovskite thin films.
Table S6. The fitting values of corresponding resistances for Nyquist plots.

3. Supplemental Methods

Supplementary TR Spectra Data Analysis

4. Supplemental References

Supplemental Figures

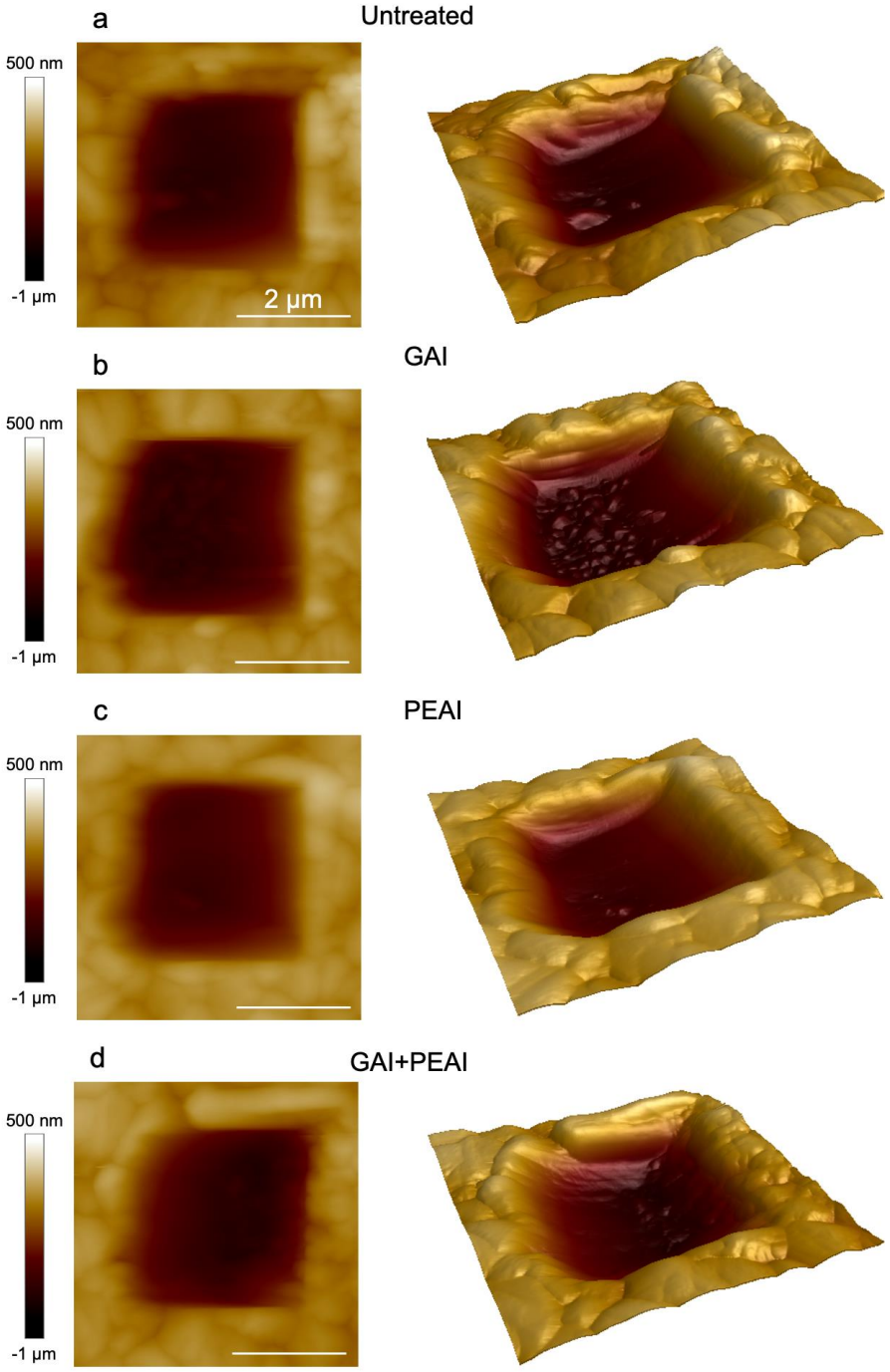

Figure S1. 2D and 3D AFM images on a 5 µm*5 µm scan of different samples after TC-AFM testing. a) Untreated; b) GAI; c) PEAI; and d) GAI+PEAI treated perovskite.

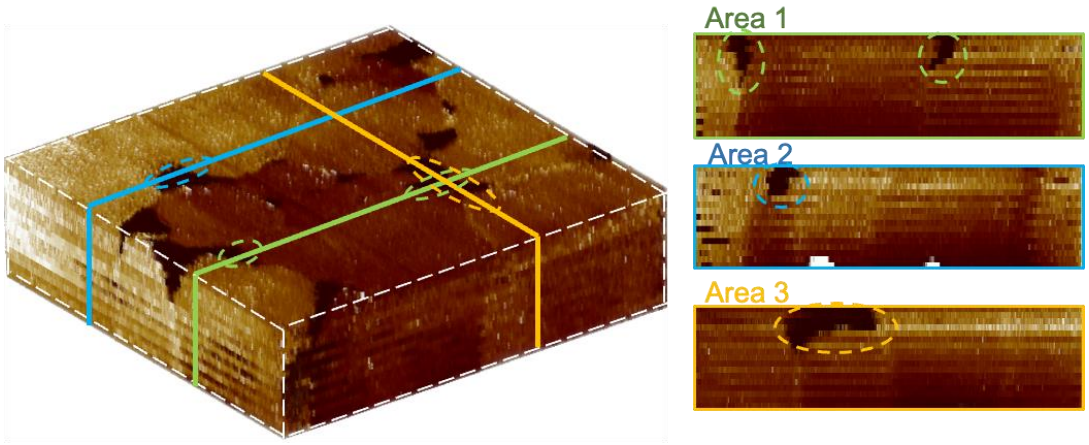

Figure S2. Three-dimensional current mapping and cross-sectional current images obtained from the C-AFM tomography experiment.

Figure S3. Experimental setup for C-AFM measurements with illumination. The perovskite film was mounted on a stage equipped with a reflective mirror, while white light from an LED source (intensity up to 1 Sun) was directed through the glass substrate onto the perovskite film. By alternating the illumination between on and off states, we obtained current mappings under both dark and illuminated conditions.

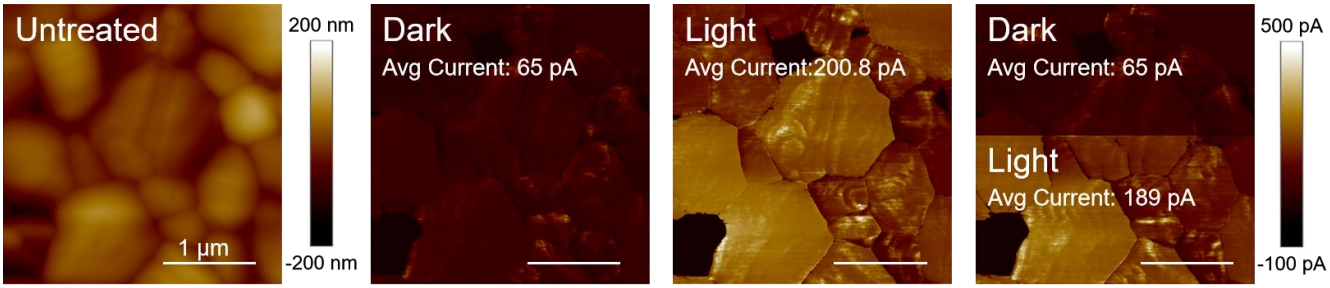

Figure S4. C-AFM images of untreated perovskite films under dark and illuminated conditions.

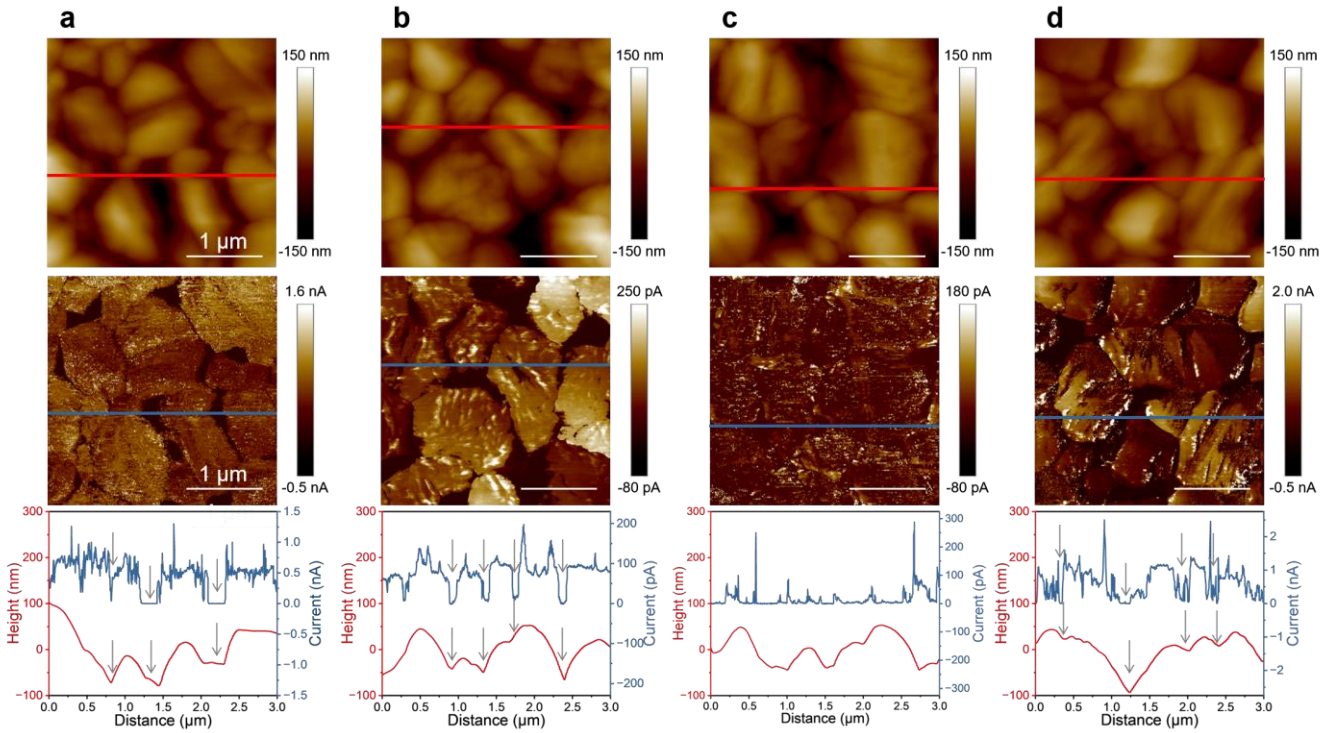

Figure S5. AFM surface images, current images, and line profiles of different perovskite samples. a) Untreated; b) GAI; c) PEAI; d) GAI+PEAI passivation.

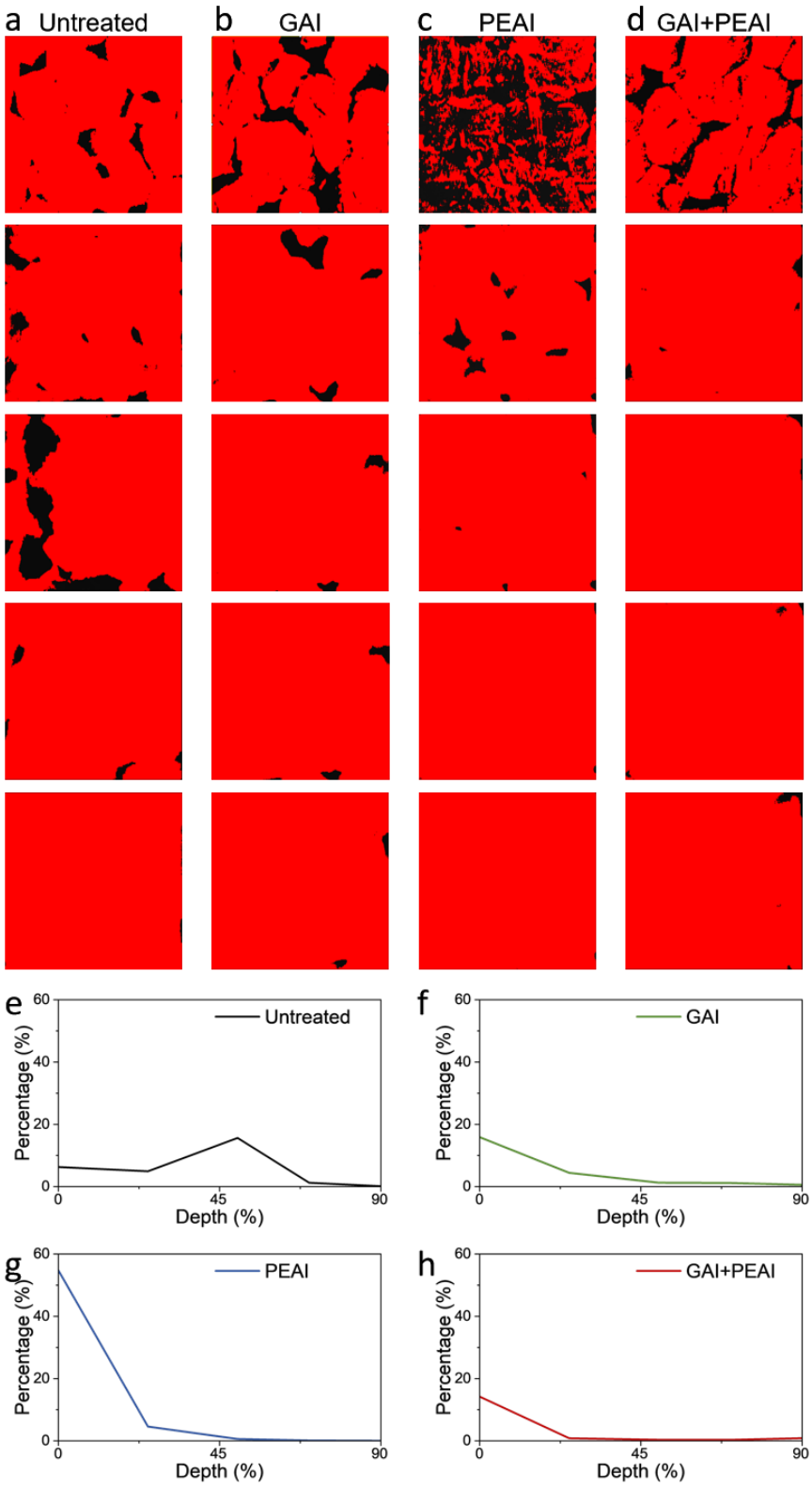

Figure S6. (a–d) Distribution of high-resistance regions at various depths for different samples, identified using ImageJ; (e–h) Changes in the fraction of high-resistance regions at different depths for each sample. The current images were converted to grayscale, and a threshold was applied to isolate high-resistance regions, which are displayed in black, from the conductive regions, shown in red.

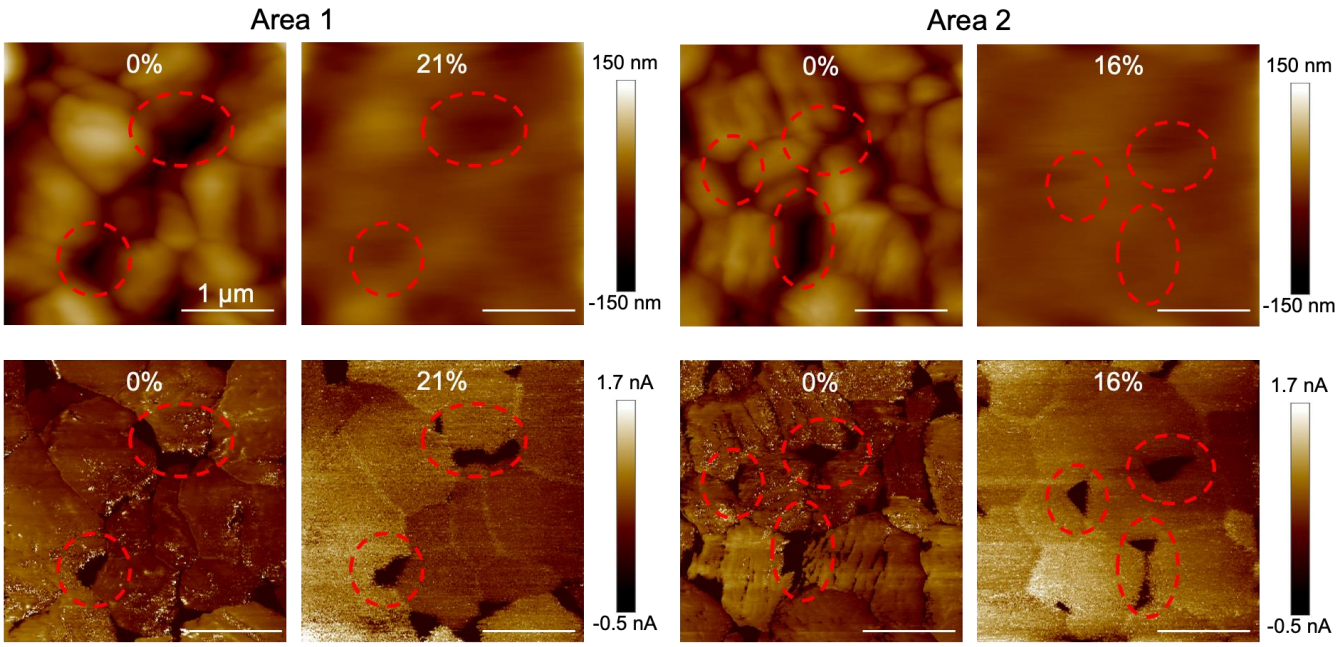

Figure S7. AFM (top) and current images (bottom) before and after removing a certain thickness.

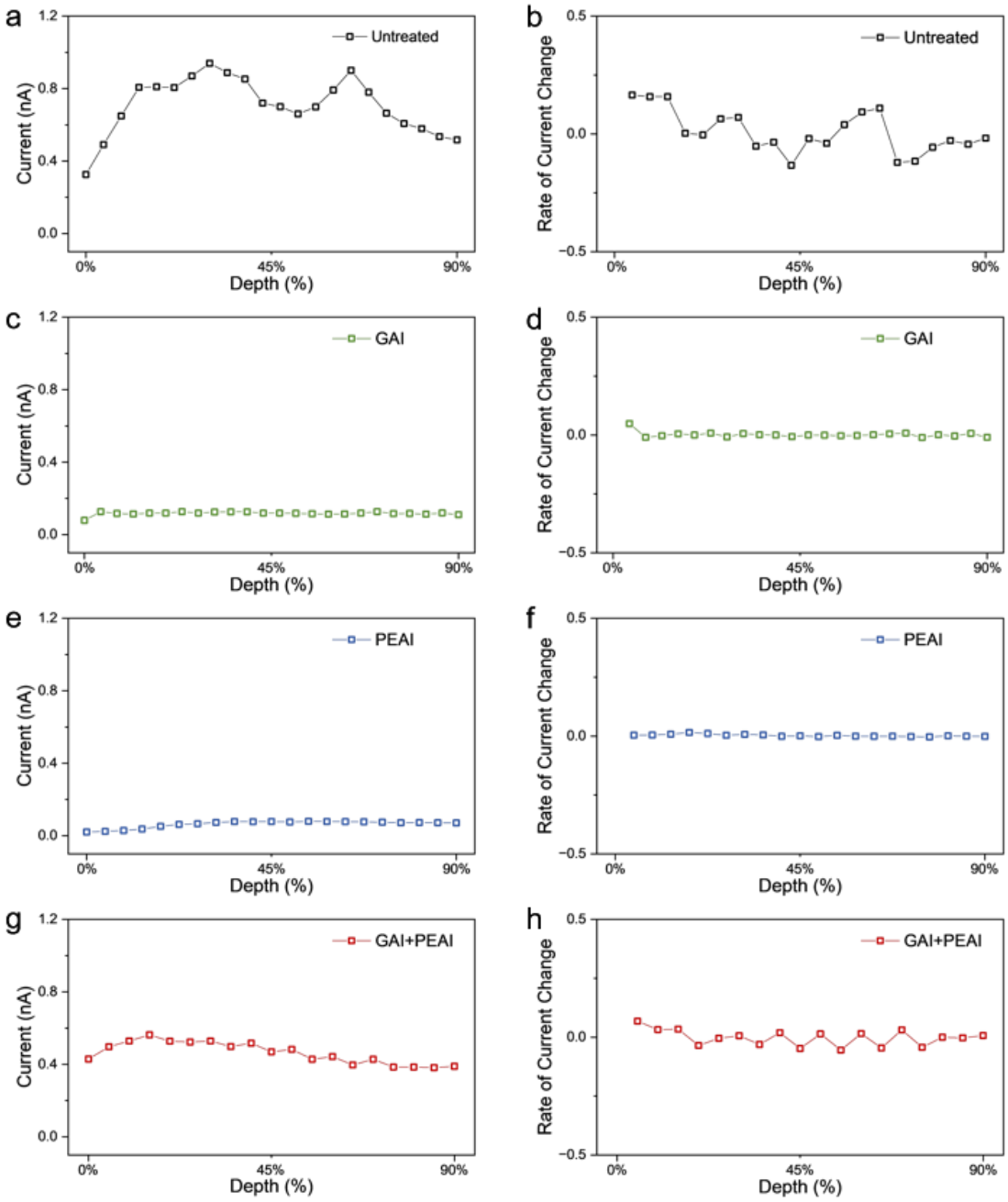

Figure S8. Depth-resolved average current variations and their rates of change for samples with different passivation treatments.

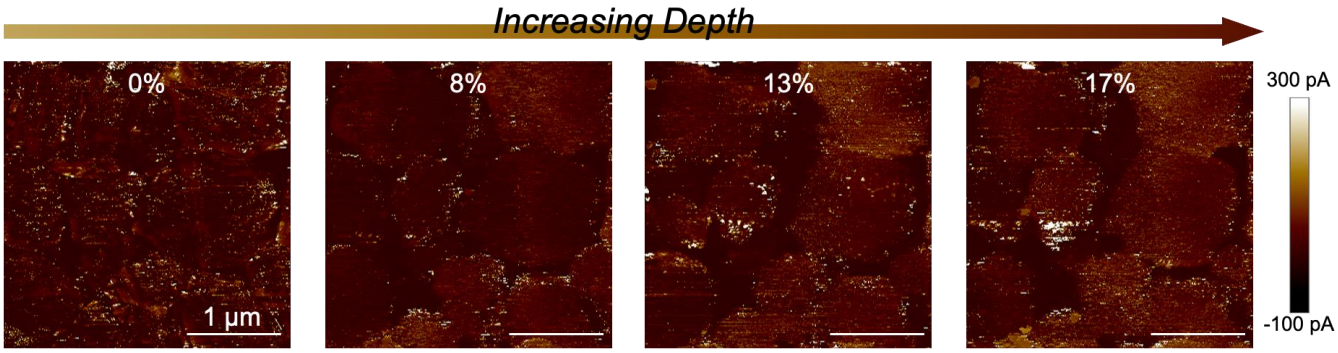

Figure S9. Sequential current images of the perovskite sample treated with PEAI passivation.

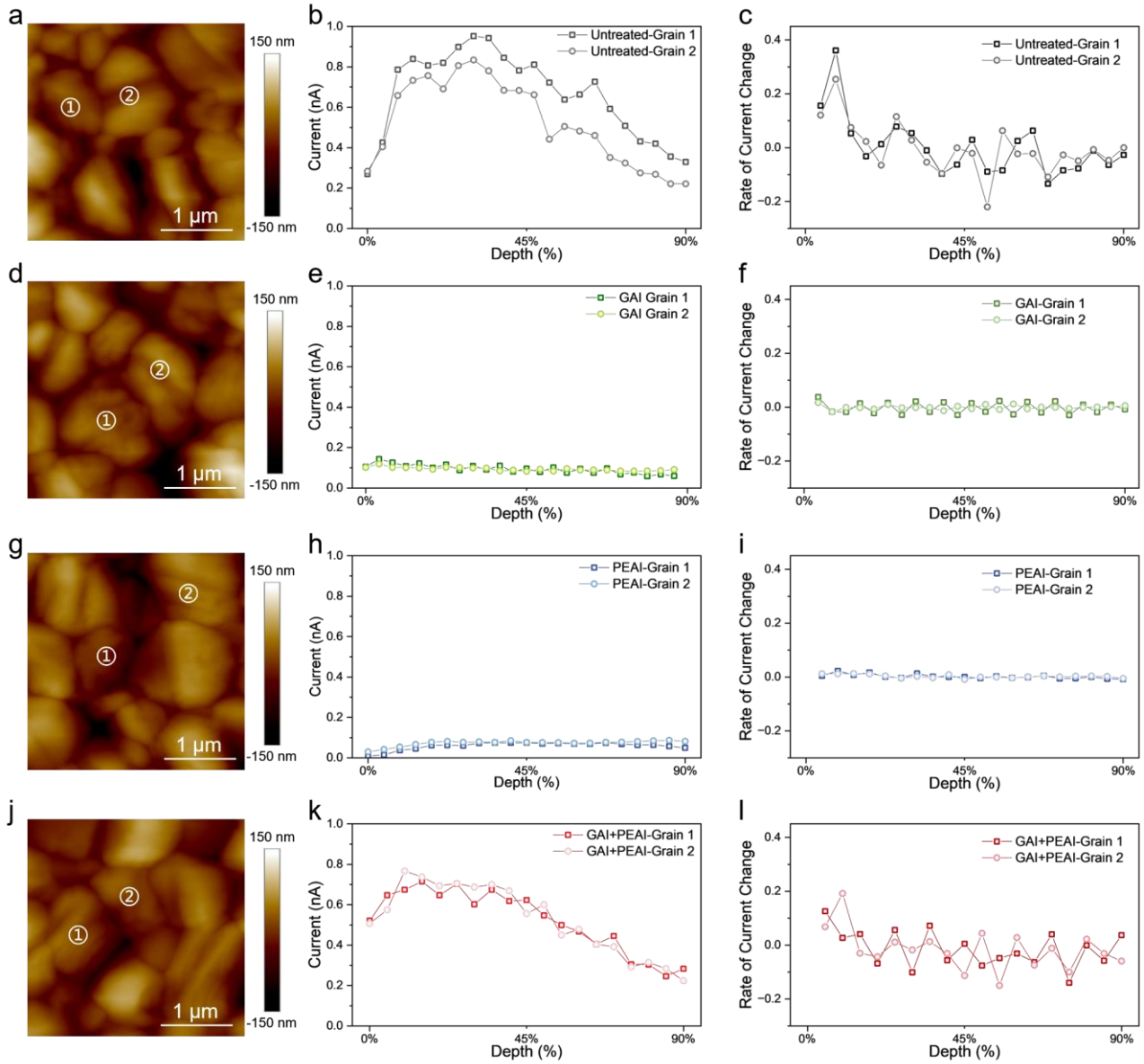

Figure S10. Depth-resolved average current and rates of change within the interiors of marked grains for perovskite films with different passivation treatments. The rates of current change were obtained by calculating the first derivative of the current profile.

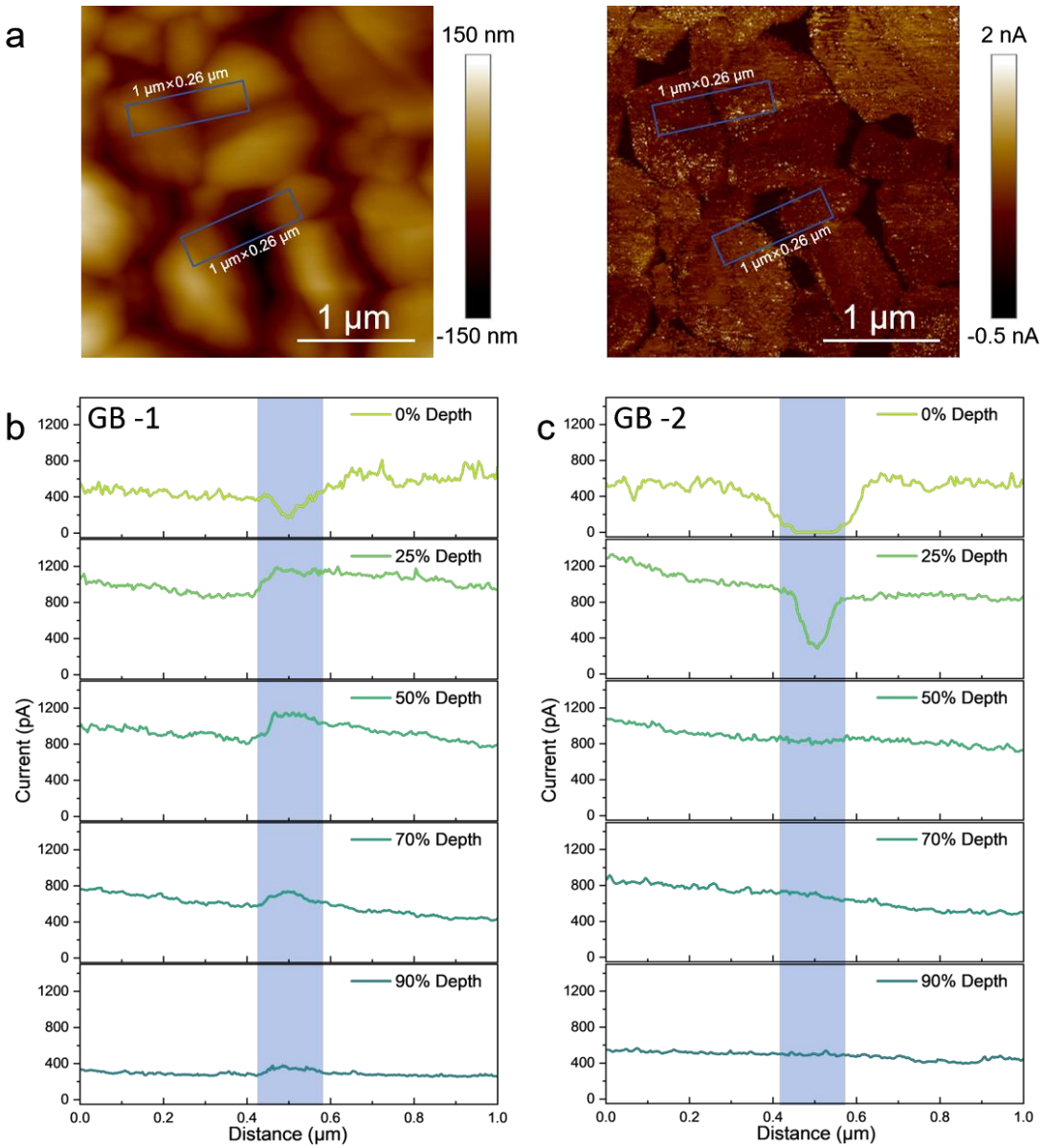

Figure S11. Depth-resolved average current of selected grain boundaries in the untreated sample. (a) AFM and C-AFM images of the sample surface, with rectangles indicating the positions of the grain boundaries and the regions used to calculate the average current; (b) and (c) Depth-resolved average current profiles for GB-1 and GB-2, respectively.

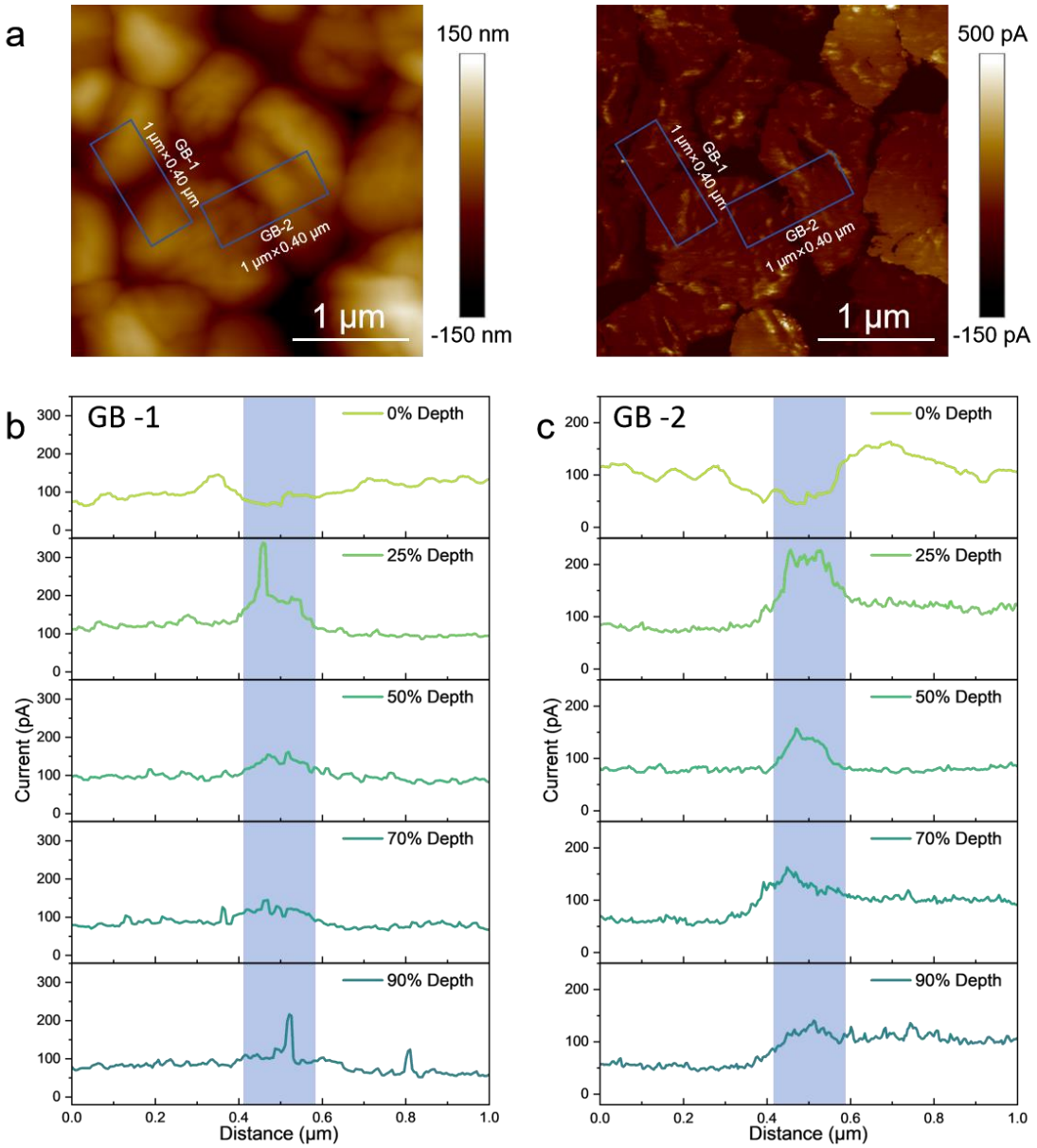

Figure S12. Depth-resolved average current of selected grain boundaries in the GAI-treated sample. (a) AFM and C-AFM images of the sample surface, with rectangles indicating the positions of the grain boundaries and the regions used to calculate the average current; (b) and (c) Depth-resolved average current profiles for GB-1 and GB-2, respectively.

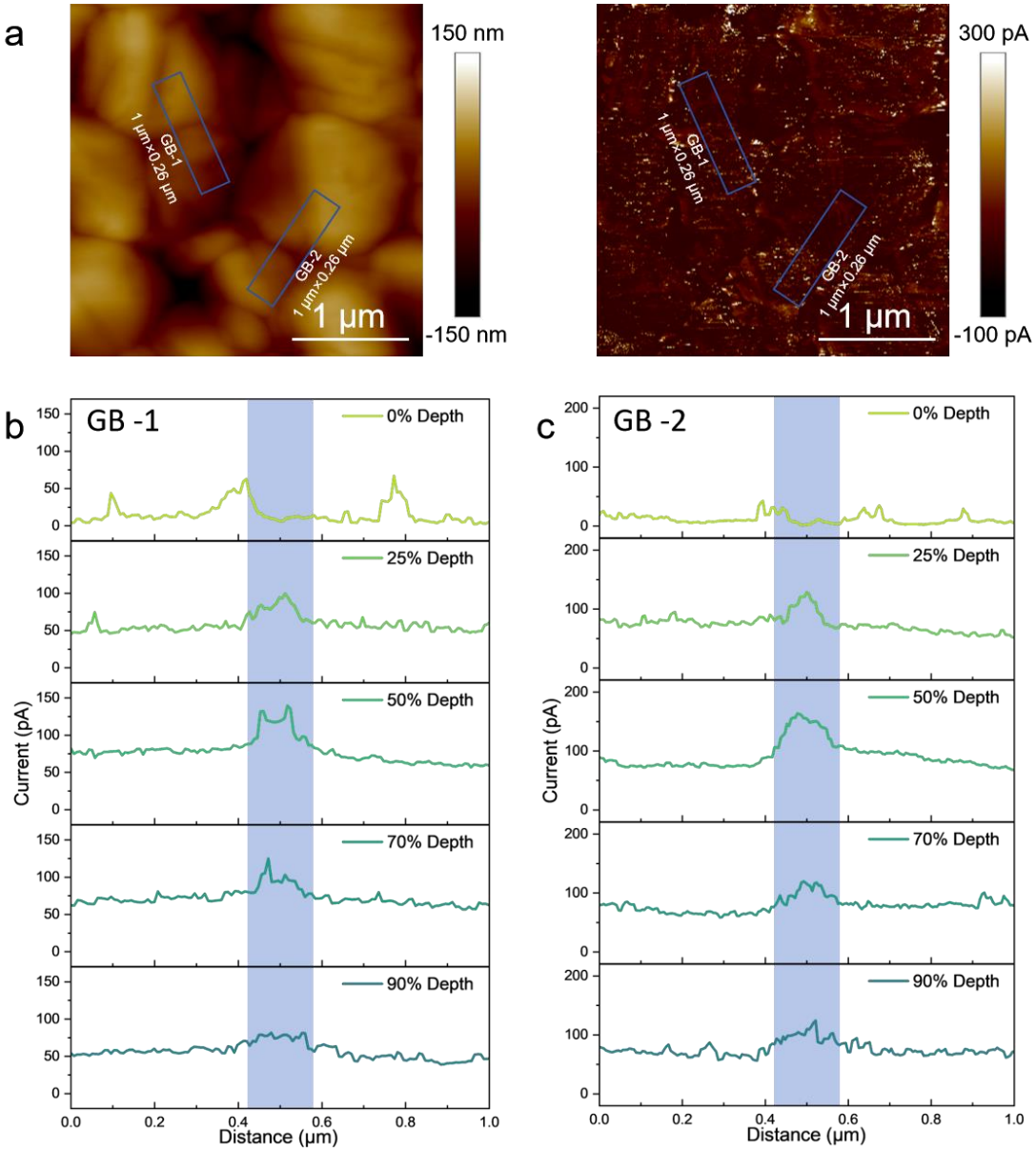

Figure S13. Depth-resolved average current of selected grain boundaries in the PEAI-treated sample. (a) AFM and C-AFM images of the sample surface, with rectangles indicating the positions of the grain boundaries and the regions used to calculate the average current; (b) and (c) Depth-resolved average current profiles for GB-1 and GB-2, respectively.

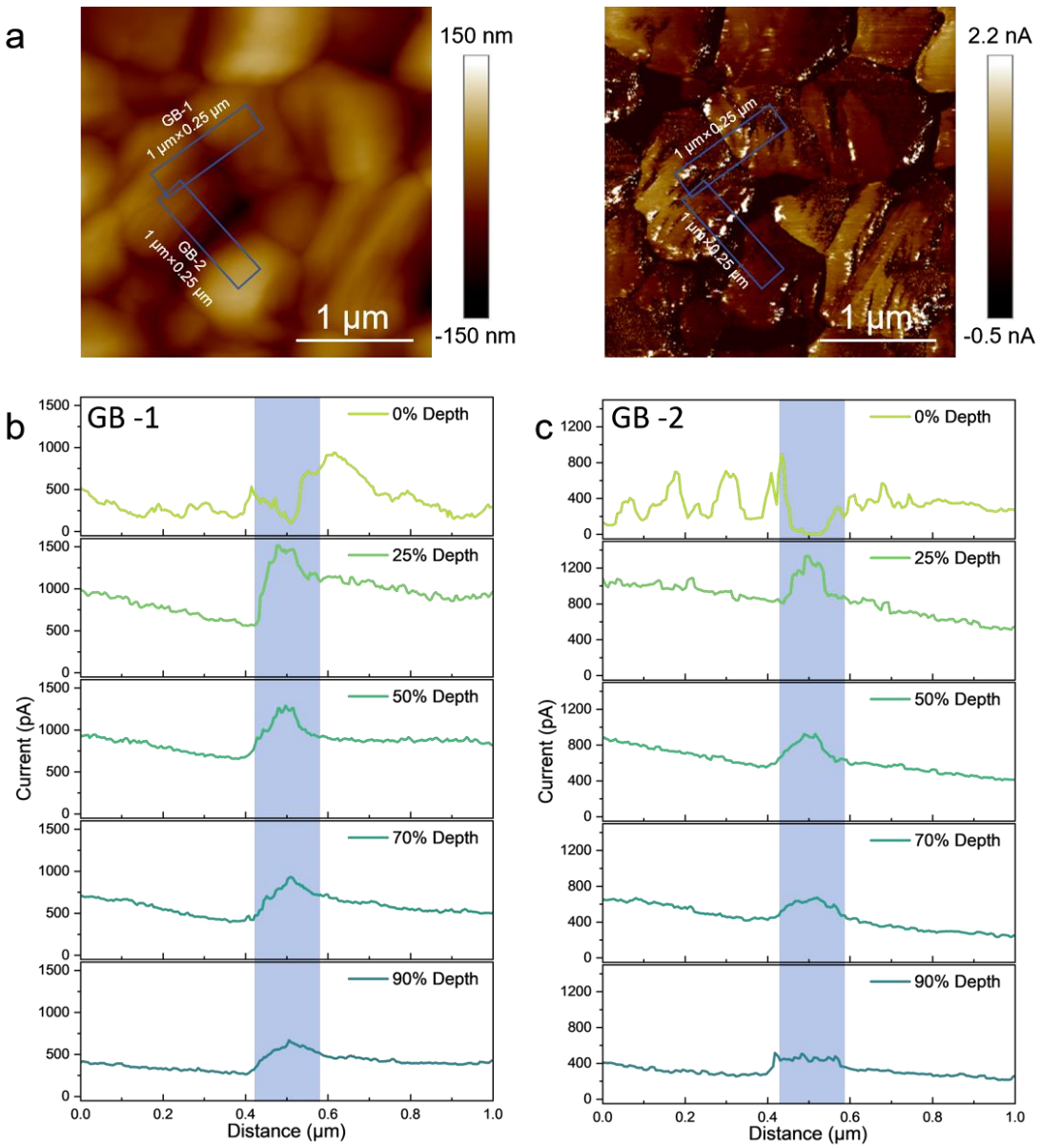

Figure S14. Depth-resolved average current of selected grain boundaries in the GAI+PEAI-treated sample. (a) AFM and C-AFM images of the sample surface, with rectangles indicating the positions of the grain boundaries and the regions used to calculate the average current; (b) and (c) Depth-resolved average current profiles for GB-1 and GB-2, respectively.

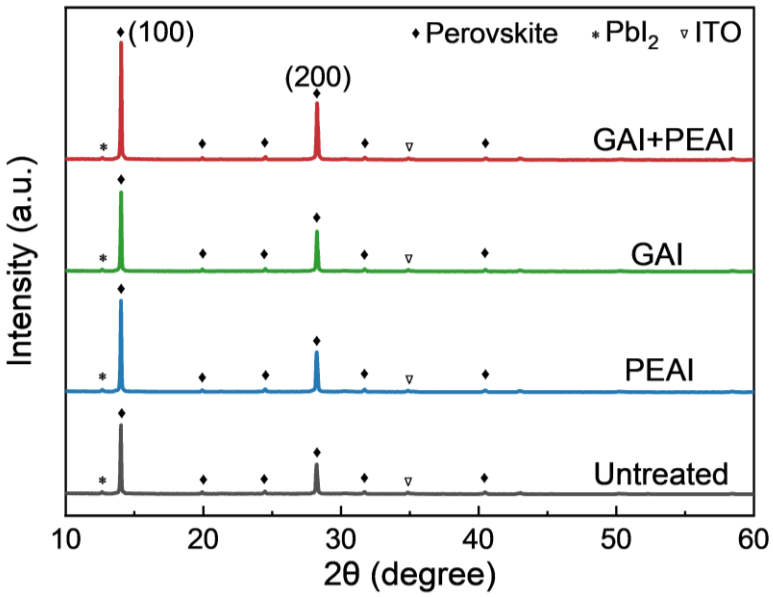

Figure S15. XRD patterns of perovskite thin films with different passivation treatments.

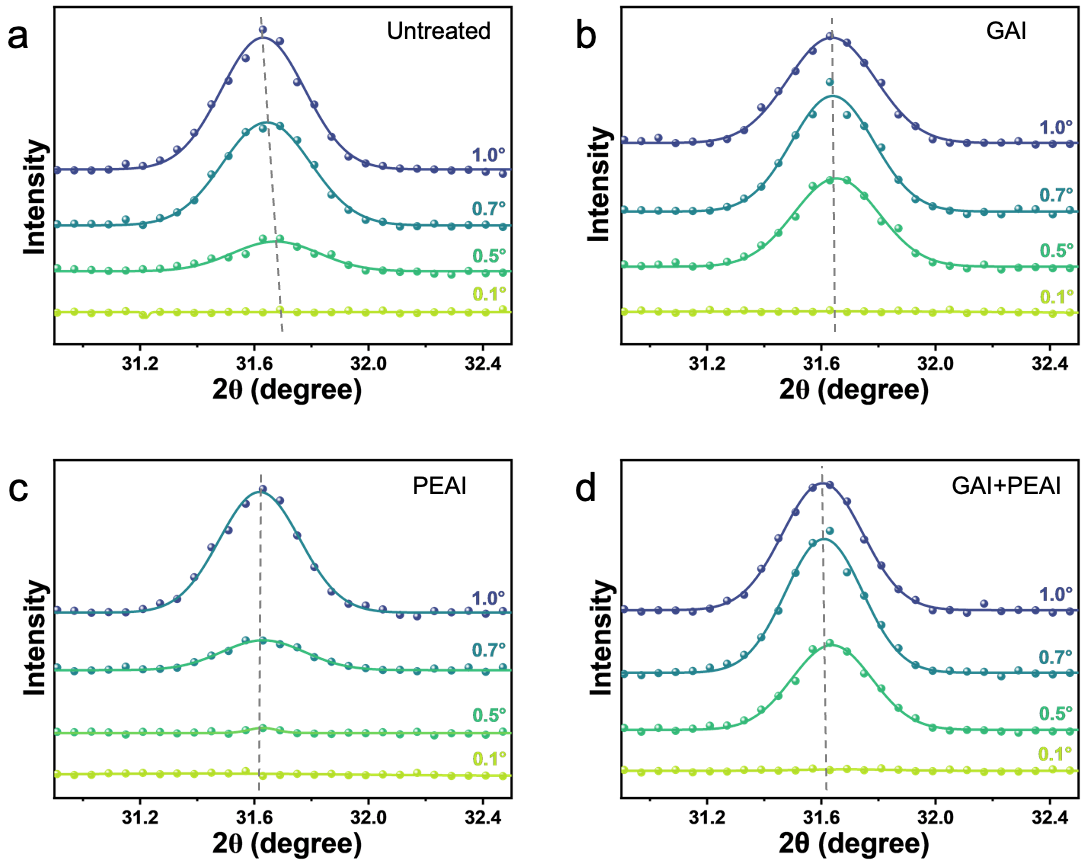

Figure S16. High diffraction angle GIXRD spectra of perovskite films measured at different grazing incidence angles. a) Untreated; b) GAI; c) PEAI; d) GAI+PEAI passivation.

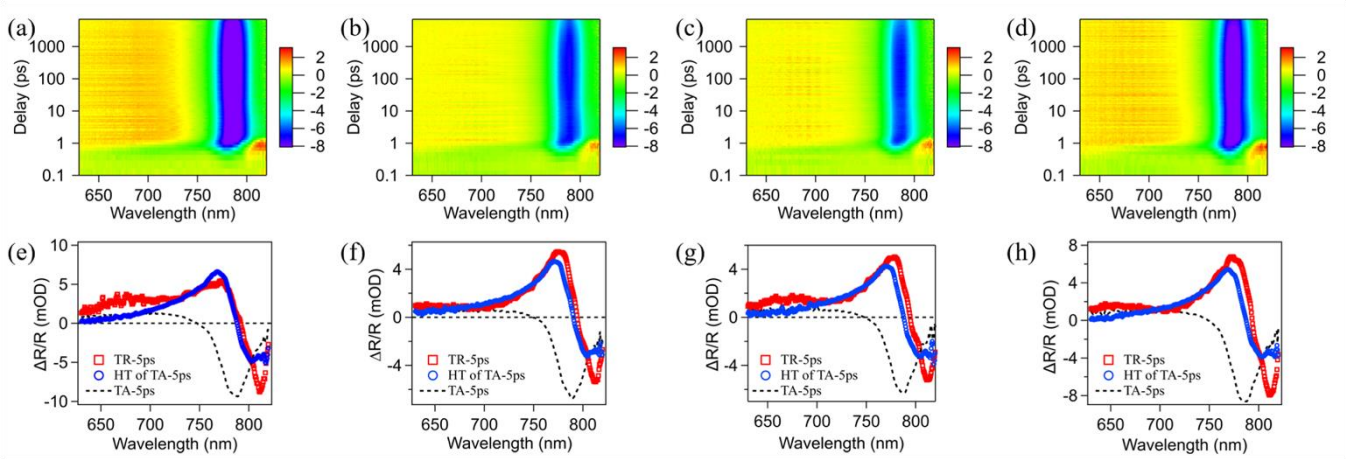

Figure S17. Two-dimensional pseudocolor maps and corresponding TA spectra at 5 ps for perovskite films with different surface treatments. (a–d) 2D pseudocolor TR maps for (a) untreated, (b) GAI-treated, (c) PEAI-treated, and (d) GAI+PEAI-treated perovskite films. (e–h) TA spectra at 5 ps corresponding to the TR signals in (a–d), shown before applying the Kramers–Kronig transformation.

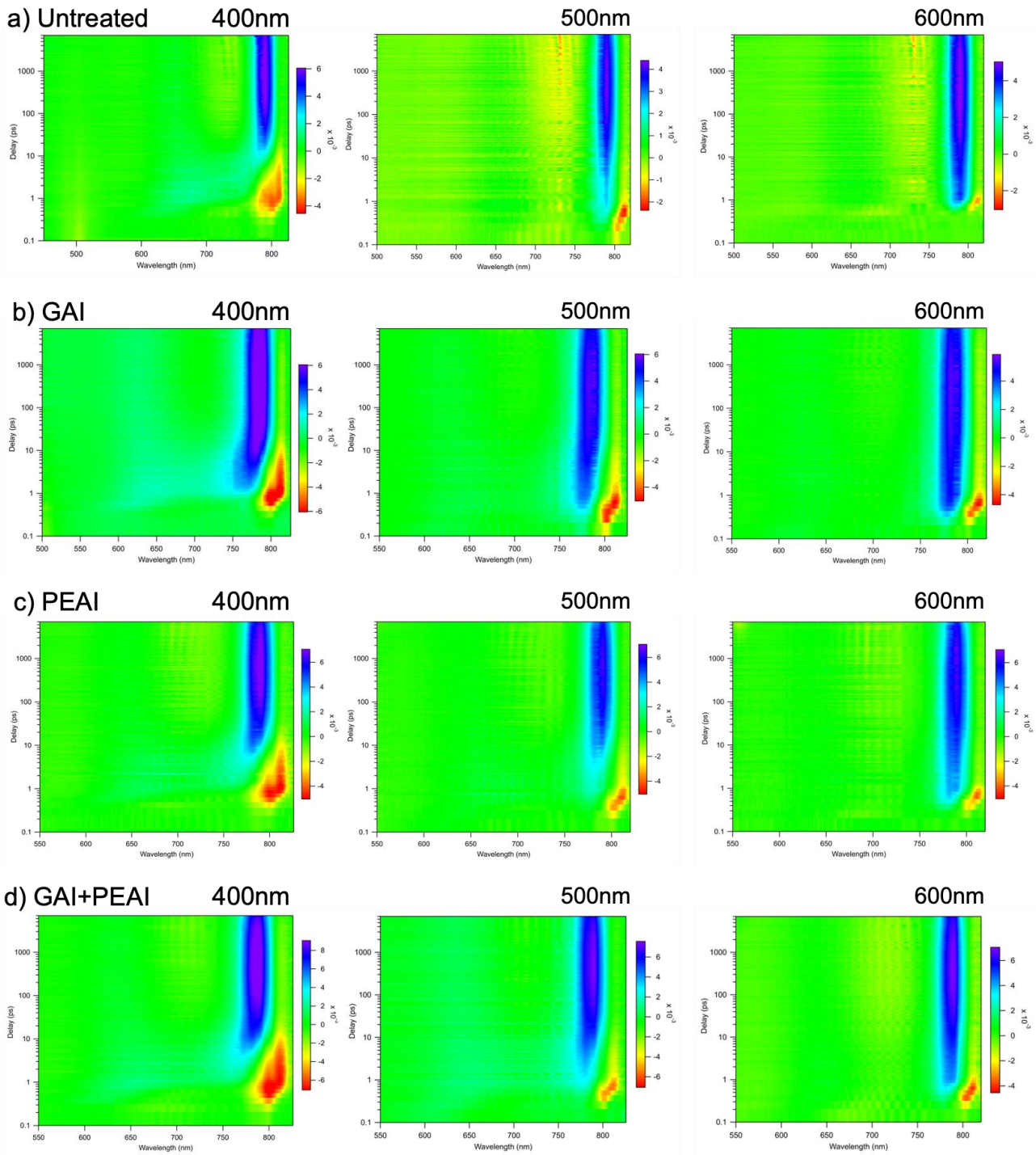

Figure S18. Two-dimensional pseudocolor images of the TR spectra of perovskite films under excitation at 400 nm, 500 nm, and 600 nm, respectively. a) Untreated; b) GAI; c) PEAI; d) GAI+PEAI passivation.

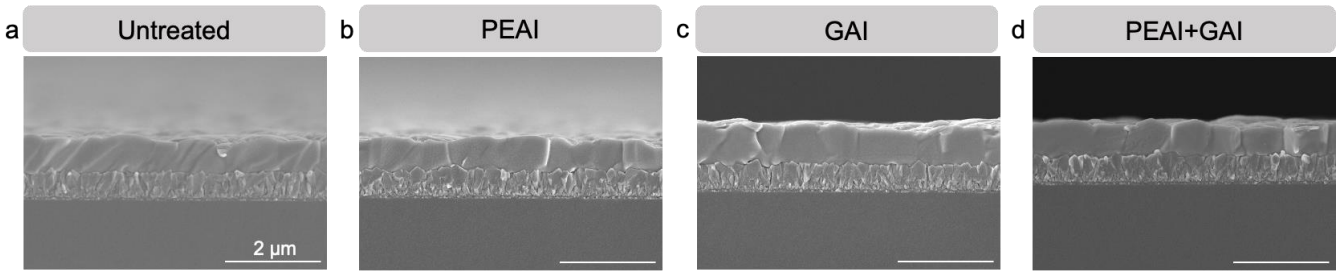

Figure S19. Cross-sectional SEM images of different perovskite samples.

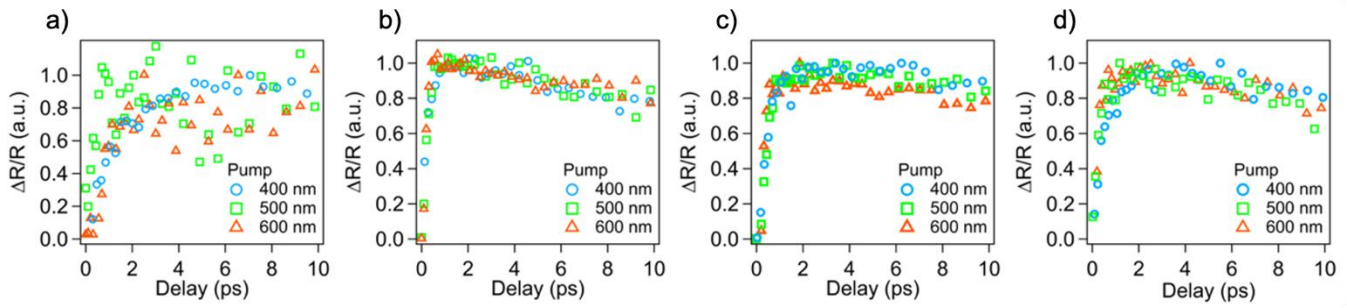

Figure S20. The TR carrier dynamics within 10 ps for the (a) untreated; (b) GAI; (c) PEAI; and (d) GAI+PEAI-treated perovskite. The corresponding probe wavelengths are (a) 765 nm, (b) 750 nm, (c) 760 nm, and (d) 755 nm.

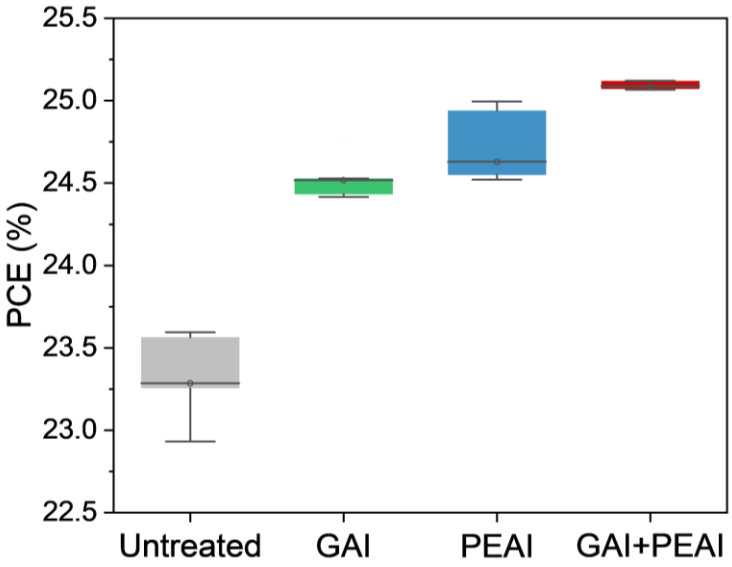

Figure S21. The statistical distribution of the PCE of the devices with different passivation treatments. The statistics are based on five devices for each treatment. Data points outside this range are shown as outliers. The median PCE values for the untreated, GAI-treated, PEAI-treated, and GAI+PEAI-treated devices are 23.3%, 24.5%, 24.7%, and 25.1%, respectively.

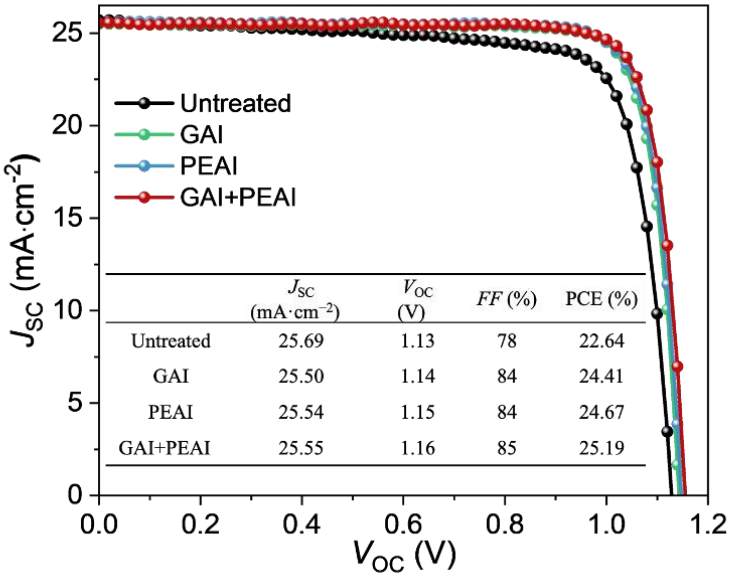

	J_{SC} (mA·cm^{-2})	V_{OC} (V)	*FF* (%)	PCE (%)
Untreated	25.69	1.13	78	22.64
GAI	25.50	1.14	84	24.41
PEAI	25.54	1.15	84	24.67
GAI+PEAI	25.55	1.16	85	25.19

Figure S22. *J-V* curves of PSCs in p-i-n structure with different passivation treatments.

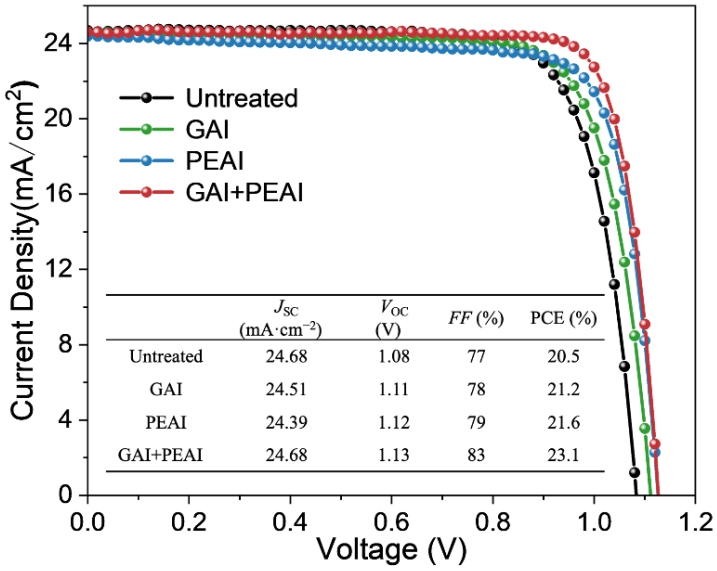

	J_{SC} (mA·cm^{-2})	V_{OC} (V)	*FF* (%)	PCE (%)
Untreated	24.68	1.08	77	20.5
GAI	24.51	1.11	78	21.2
PEAI	24.39	1.12	79	21.6
GAI+PEAI	24.68	1.13	83	23.1

Figure S23. *J-V* curves of PSCs in n-i-p structure with different passivation treatments.

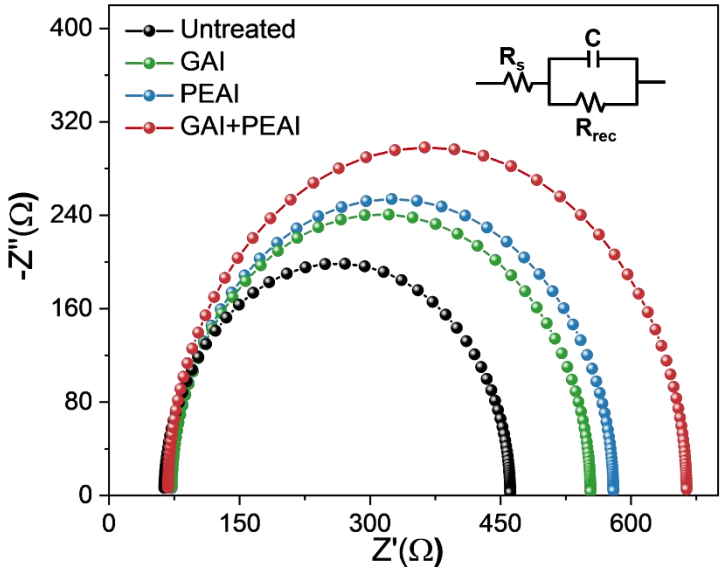

Figure S24. Nyquist plots for different samples.

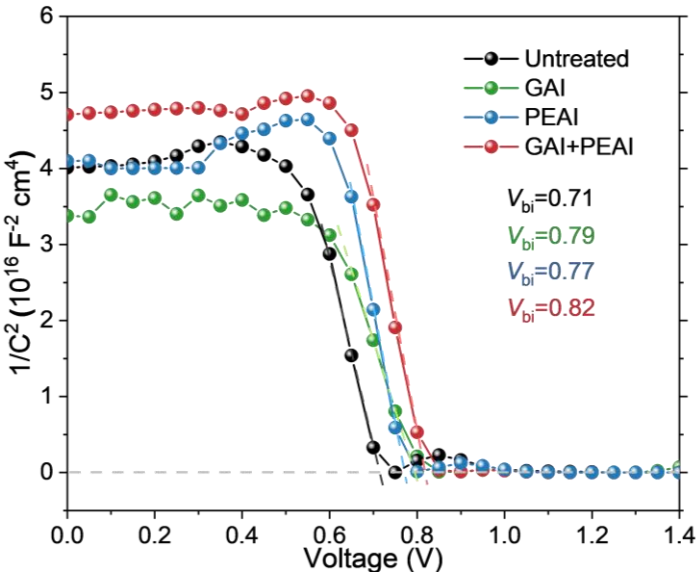

Figure S25. Mott-Schottky curves for different samples.

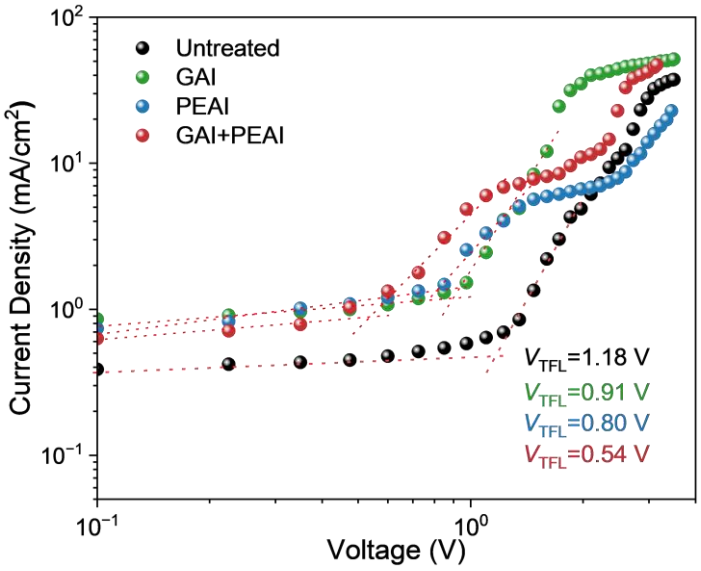

Figure S26. SCLC characteristics of hole-only devices for the untreated and passivated samples. Trap density N_t is calculated using the formula[2,3]: $N_t = \frac{2\varepsilon_r\varepsilon_0 V_{TEL}}{eL^2}$, where ε_r is the relative permittivity of $FAPbI_3$[4], ε_0 is the vacuum permittivity (8.854 × 10^{-12} F/m), e is the electron charge (1.6 × 10^{-19} C), and L is the thickness of the perovskite film (700 nm).

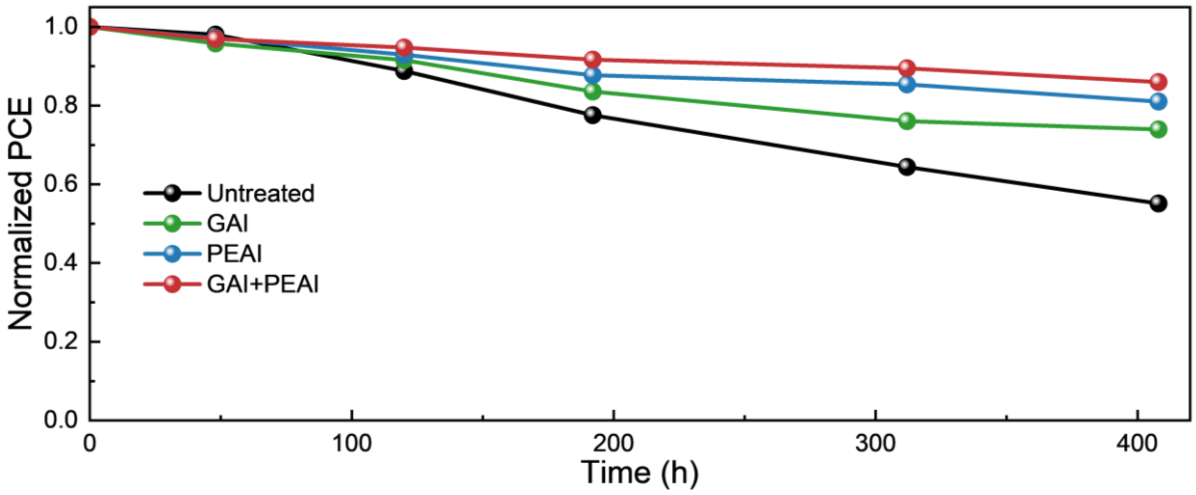

Figure S27. Normalized PCE variation curves of the devices in air (RH=20-50%; room temperature).

Supplemental Tables

Table S1. Fractions of high-resistance regions at different depths for samples with different passivation treatments.

	0% Depth	25% Depth	50% Depth	70% Depth	90% Depth
Untreated	6.30	4.92	15.63	1.26	0.15
GAI	15.89	4.43	1.27	1.18	0.59
PEAI	54.76	4.11	0.62	0.52	0.03
GAI+PEAI	14.22	0.86	0.35	0.33	0.87

Table S2. Ratios of grain boundary current to grain interior current for selected grain boundaries in different samples.

	0% Depth	25% Depth	50% Depth	70% Depth
Untreated GB-1	124%	120%	119%	128%
Untreated GB-2	40%	97%	86%	97%
GAI GB-1	174%	170%	152%	175%
GAI GB-2	265%	184%	231%	228%
PEAI GB-1	186%	157%	154%	147%
PEAI GB-2	183%	210%	180%	163%
GAI+PEAI GB-1	209%	174%	197%	191%
GAI+PEAI GB-2	144%	147%	144%	190%

Table S3. The extracted peak height ratios of (001)/PbI_2 and (002)/PbI_2.

	(001) Peak Ratio	(002) Peak Ratio
Untreated	32.65	14.07
GAI	47.44	20.82
PEAI	39.44	20.03
GAI+PEAI	59.26	27.01

Table S4. Pump photon energy and average carrier density used for the TR measurements of the four samples.

	Photon Energy (eV)	Average carrier density (cm^{-3})
Untreated	3.10	2.95×10^{17}
	2.25	2.30×10^{17}
	2.07	2.80×10^{17}
GAI-treated	3.10	3.95×10^{17}
	2.48	3.38×10^{17}
	2.25	3.31×10^{17}
PEAI-treated	3.10	2.70×10^{17}
	2.48	3.62×10^{17}
	2.25	2.68×10^{17}
GAI+PEAI-treated	3.10	3.49×10^{17}
	2.48	2.97×10^{17}
	2.25	3.78×10^{17}

Table S5. Fitted diffusion coefficients and surface recombination rates for the untreated, GAI, PEAI, and GAI+PEAI-treated perovskite thin films.

	S (10^3 cm/s)	D (cm^2/s)
Untreated	0.66±0.09	1.16±0.21
GAI	0.55±0.12	1.38±0.18
PEAI	0.33±0.14	1.04±0.25
GAI+PEAI	0.23±0.10	1.35±0.15

Table S6. The fitting values of corresponding resistances for Nyquist plots.

	R_S (Ω)	R_{rec} (Ω)
Untreated	63.84	460.44
GAI	72.30	553.49
PEAI	72.78	578.86
GAI+PEAI	67.35	664.25

Supplemental Methods

Supplementary TR Spectra Data Analysis

Carrier Density vs. Transient Reflection Signals

Near the semiconductor bandgap, the real part of the refractive index (n) dominates over the imaginary part (k), so the pump-induced reflectance change ΔR/R mainly reflects the modulation of n by photocarriers. Because the probe penetrates only ~10-50 nm, depending on the refractive index of the material, TR spectroscopy is sensitive to carriers near the interface.

At low carrier density, the change in reflectivity measured by TR is proportional to the real part of the refractive index Δn,

$$\frac{\Delta R}{R}(\hbar\omega) \cong \frac{4}{n(\hbar\omega)^2-1} \times \Delta n(\hbar\omega) \quad \text{(S-1)}$$

The change of refractive index Δn can be related to the change of absorption coefficient $\Delta\alpha$ through the Kramers-Kronig relationship:

$$\Delta n(\hbar\omega) = \frac{c}{\pi} P \int_0^{+\infty} \frac{\Delta\alpha(\hbar\omega)}{\omega_1^2-\omega^2} d\omega_1 \quad \text{(S-2)}$$

where c is the speed of light and *P* is the Cauchy principal value of the integral.

At low carrier density, $\Delta\alpha$ can be associated with the carrier density:

$$\Delta\alpha(\hbar\omega) = \alpha_0(\hbar\omega) \times \frac{N}{N_m} \quad \text{(S-3)}$$

where N is the carrier density induced by the pump pulse, and N_m is the saturation charge density (approximately 10^{19} cm^{-3}). Here, we maintain our pump intensity at approximately 10^{17} cm^{-3}. Therefore, in the surface region, ΔR/R, the decay $N(x,t)|_{t=0}$ can be directly tracked.

One-Dimensional Diffusion Model

At the semiconductor surface, the dominant carrier dynamics involve carrier diffusion out of the probed region and surface recombination. As photon energy increases, higher-energy pump photons enhance the initial carrier density gradient, thereby accelerating the surface decay dynamics due to an increased diffusion rate. To quantitatively describe the evolution of carrier density under different optical excitation conditions, a one-dimensional diffusion equation was employed for modeling and analysis, as follows.

$$\frac{\partial N(x,t)}{\partial t} = D\frac{\partial^2 N(x,t)}{\partial x^2} - \frac{N(x,t)}{\tau_B} \quad \text{(S-4)}$$

where N(x, t) is the function of carrier density with depth (x) and time (t), D is the diffusion coefficient, and τ_B is the lifetime of bulk carriers.

The initial carrier distribution is governed by the Lambert-Beer law:

$$N(x,t)|_{t=0} = N_0 e^{-\alpha x} \quad \text{(S-5)}$$

where α is the absorption coefficient that varies with the energy of the pump photons, resulting in different penetration depths for different pump energies.

The recombination of carriers on the surfaces can be described as follows:

$$\left.\frac{\partial N(x,t)}{\partial t}\right|_{x=0/L_{PC}} = \frac{S}{D} N(0,t) \quad \text{(S-6)}$$

where S represents the recombination velocities at the surfaces. By integrating the above equations, a surface carrier dynamics model can be established, enabling the determination of the diffusion coefficient (D) and the surface recombination velocity (S). This method is adapted from supplemental reference 1.

Supplemental References

[S1] Yang, Y., Yang, M., Moore, D.T., Yan, Y., Miller, E.M., Zhu, K., and Beard, M.C. (2017). Top and bottom surfaces limit carrier lifetime in lead iodide perovskite films. Nat. Energy 2, 16207. 10.1038/nenergy.2016.207.

[S2] Targhi, F.F., Jalili, Y.S., and Kanjouri, F. (2018). $MAPbI_3$ and $FAPbI_3$ perovskites as solar cells: Case study on structural, electrical and optical properties. Res. Phys. 10, 616–627. 10.1016/j.rinp.2018.07.007.

[S3] Heo, J.H., Park, J.K., Lee, H.J., Shin, E.H., Hong, S.Y., Hong, K., Zhang, F., and Im, S.H. (2024). Inorganic-derived 0D perovskite induced surface lattice arrangement for efficient and stable all-inorganic perovskite solar cells. Adv. Mater. 36, 2408387. 10.1002/adma.202408387.

[S4] Han, Q., Bae, S., Sun, P., Hsieh, Y., Yang, Y. (Michael), Rim, Y.S., Zhao, H., Chen, Q., Shi, W., Li, G., et al. (2016). Single crystal formamidinium lead iodide ($FAPbI_3$): insight into the structural, optical, and electrical properties. Adv. Mater. 28, 2253–2258. 10.1002/adma.201505002.